https://doi.org/10.1016/j.jmst.2021.09.029

This is the Pre-Published Version.

Laser surface treatment-introduced gradient nanostructured TiZrHfTaNb refractory high-entropy alloy with significantly enhanced wear resistance

Jiasi Luo[a,b], Wanting Sun[a], Ranxi Duan[b], Wenqing Yang[a], K. C. Chan[a], Fuzeng Ren[b*], and Xu-Sheng Yang [a,c*]

[a]Advanced Manufacturing Technology Research Centre, Department of Industrial and Systems Engineering, The Hong Kong Polytechnic University, Hung Hom, Kowloon, Hong Kong, China

[b]Department of Materials Science and Engineering, Southern University of Science and Technology, Shenzhen, Guangdong 518055, China

[c]The Hong Kong Polytechnic University Shenzhen Research Institute, Shenzhen, Guangdong 518060, China

[*] Corresponding author: xsyang@polyu.edu.hk (X.-S Yang); renfz@sustech.edu.cn (F.Z. Ren)

© 2022. This manuscript version is made available under the CC-BY-NC-ND 4.0 license http://creativecommons.org/licenses/by-nc-nd/4.0/

Abstract

Heterogeneous gradient nanostructured metals have been shown to achieve the strength-ductility synergy, thus potentially possessing the enhanced tribological performance in comparison with their homogeneous nanograined counterparts. In this work, a facile laser surface remelting-based surface treatment technique is developed to fabricate a gradient nanostructured layer on a TiZrHfTaNb refractory high-entropy alloy. The characterization of the microstructural evolution along the depth direction from the matrix to the topmost surface layer shows that the average grain size in the ~ 100 μm-thick gradient nanostructured layer is dramatically refined from the original ~ 200 μm to only ~ 8 nm in the top surface layer. The microhardness is therefore gradually increased from ~ 240 HV in matrix to ~ 650 HV in the topmost surface layer, approximately 2.7 times. Noticeably, the original coarse-grained single-phase body-centered-cubic TiZrHfTaNb refractory high-entropy alloy is gradually decomposed into TiNb-rich body-centered-cubic phase, TaNb-rich body-centered-cubic phase, ZrHf-rich hexagonal-close-packed phase and TiZrHf-rich face-centered-cubic phase with gradient distribution in grain size along the depth direction during the gradient refinement process. As a result, the novel laser surface treatment-introduced gradient nanostructured TiZrHfTaNb refractory high-entropy alloy demonstrates the significantly improved wear resistance, with the wear rate reducing markedly by an order of magnitude, as compared with the as-cast one. The decomposed multi-phases and gradient nanostructures should account for the enhanced wear resistance. Our findings provide new insights into the refinement mechanisms of the laser-treated refractory high-entropy alloys and broaden their potential applications via heterogeneous gradient nanostructure engineering.

Keywords: Laser surface treatment, refractory high-entropy alloy, gradient nanostructure, wear resistance, high-resolution transmission electron microscopy

1. Introduction

Metallic alloys with superior mechanical properties are always in demand for various functional and structural applications. Over the past decade, a new philosophy has been proposed to design the high-entropy alloys (HEAs) with equimolar or near-equimolar fractions of multiple constituents [1, 2]. This breakthrough concept arises from the maximum configurational entropy of multi-component solid solution, which consequently stabilizes the disordered solid-solution phases rather than the traditional intermetallic phases [3]. As a result, the unique HEAs have demonstrated numerous interesting properties for multifarious potential applications [4, 5]. In particular, refractory HEAs (RHEAs), which is primarily designed through selecting refractory elements with high melting points [6], can demonstrate high structural stability and notable mechanical strength at elevated temperatures. For example, NbMoTaW and VNbMoTaW RHEAs have shown the exceptional strength at temperatures above 1000 ^{o}C, even compared with some conventional superalloys and their compositional derivatives [7]. A single body-centered cubic (BCC) solid-solution can be maintained in the 1000 ^{o}C-annealed TiZrHfTaNb RHEA, exhibiting extraordinary mechanical properties (*e.g.* yield stress of 800-1000 MPa and compressive strain exceeding 50% [8]).

Uniformly reducing the grain size to the nanometer scale (< 100 nm) has been well recognized to substantially improve the strength and hardness of metals, as described by the empirical Hall-Petch relation [9, 10]. However, hardened homogenous nanograined (NG) metals (even those that are very ductile in their coarse-grained (CG) counterparts) normally have extremely poor ductility [11]. Due to the significantly reduced grain size and increased grain boundaries (GBs), the plasticity controlled by the dislocations multiplication and motion are severely limited in NG metals, leading to the mechanical instability and thus no improvement in tribological properties [12], especially under the high-load (or speed) sliding condition [13, 14]. For example, the relatively high coefficient of friction (COFs) with surface roughening and delaminating are often observed in NG metals during the wear testing [15].

Alternatively, the mechanical instability can be apparently alleviated in a heterogeneous gradient nanostructure (GNS), *e.g.* where phase, grain size and/or twin thickness are gradually distributed/decreased from the top surface to the interior [16-22]. GNS can be fabricated via various surface severe plastic deformation (SSPD) techniques, such as surface mechanical

grinding treatment [23-26], surface mechanical attrition treatment [27, 28], high pressure torsion (HPT) [29, 30], and high-speed machining [31, 32], etc., in which the most severe plastic strain and strain rate are caused in the top surface and then gradually decreased toward the interior of the specimens. The multi-scale strain/stress partitioning along the gradient direction can be harvested to achieve the strength-ductility synergy [33]. For instance, HPT-processed TiZrHfTaNb RHEA showed a significant increase in tensile strength (up to ~ 1900 MPa) and well-retained ductility [34]. In contrast to NG metals, it should be noticed that GNS can effectively suppress the strain localization and accommodate the large plasticity to prevent the surface roughening and delaminating, thereby demonstrating the significantly enhanced wear resistance [26]. For instance, the obvious lower dry-sliding COFs was reported in GNS Cu-Ag alloy[15, 26].

Owing to the characteristics of high-energy density, high controllability and flexibility, and precision [35-37], an advanced technique named laser surface treatment has been developing to fabricate GNS metals with uncertain dimensions and complex shapes. Specifically, laser surface treatment techniques include laser shock peening (LSP), laser surface re-melting (LSR), and laser surface quenching (LSQ). During the LSP process, high-energy laser pulses generate the high-pressure shockwave (exceeding yield strength) in the near surface of the specimen, thus producing ultra-high plastic strain along the depth direction for forming the GNS. For example, Tong *et al*.[38] reported the gradient refinement process of a thick GNS CoCrFeMnNi HEA layer when subjected to LSP process, and dislocation walls, concurrent nanobands and mechanical twins, and NGs along the depth direction were observed. Whereas, the gradient refinement mechanisms by the LSR and LSQ are related to the high-power laser beam-induced rapid heating and cooling processes (*e.g.* with an order of 10^5–10^8 K/s), which generate the ultra-high thermal and residual plastic strains during the solidification in LSR and self-quenching in LSQ processes along the depth direction of the specimens. The ultra-high temperature produced by laser treatment also provides a great possibility for the nucleation of new phases. However, the whole cooling process only last tens of milliseconds, which is too short to allow nano-sized nuclei of the newly formed phases to grow up. As a result, the processes of LSR and LSQ can also obtain GNS HEAs for improving the mechanical properties. For example, the grain refinement was evidenced in the LSR-processed Ti-35Nb-

2Ta-3Zr alloy, which showed the obviously increased surface mechanical properties [39].

The above findings indicate that GNS metals produced by the laser surface treatment can effectively improve the strength-ductility synergy and particularly the wear resistance. In contrast to the traditional alloys and HEAs, the refectory element constituted-RHEAs can have some distinct characteristics, including lattice distortion, chemical bonds, phase constitutions/transformations, dislocation behaviors, and thermal conductivity [40, 41], etc., which might lead to the different plastic behavior governing the gradient refinement during the LSR heating and cooling processes and corresponding tribological properties. To our best knowledge, however, it is still quite limited literature to investigate these two critical issues of the laser surface treated-HEAs, especially the RHEAs. Herein, an LSR-based laser surface treatment technique is developed to fabricate the GNS layer on TiZrHfTaNb alloy (*i.e.* one of the most promising RHEAs) with a thickness of ~ 100 μm, in which the average grain size is effectively refined from the original ~ 200 μm to only ~ 8 nm in the topmost surface layer. More specifically, high-resolution transmission electron microscopy (HRTEM) was mainly performed to dissect the microstructural evolution along the depth direction from the matrix region to the top surface layer, discovering the phase decomposition-involved gradient refinement mechanism. In addition to the surface hardness increased by ~ 2.7 times, the novel laser surface treated- GNS TiZrHfTaNb RHEA shows the significantly enhanced tribological properties with a reduction in wear rate by an order of magnitude. Our findings provide new insights into the refinement mechanism of the TiZrHfTaNb alloy subjected to the LSR process and broaden their potential applications via heterogeneous gradient nanostructuring.

2. Experimental

2.1. Material preparation and laser surface treatment

The equimolar mixtures of refectory elements (*i.e.* Ti, Zr, Hf, Ta, and Nb) with the purities over 99.9 wt.% were prepared to fabricate the TiZrHfTaNb RHEA ingots by vacuum arc melting, which was repeated for six times to achieve the homogeneous distribution. The ~ 10 mm-thick as-cast alloy was then sliced by electric discharge machining (EDM) into samples with dimensions of 30 mm × 30 mm × 2 mm. Subsequently, these samples were mechanically polished using SiC papers to obtain the plate specimens with a thickness of ~1.5 mm.

To avoid surface oxidation during the generation of the GNS layer, the continuous zigzag-path laser surface treatment process was completed on the as-cast plate specimens by using the 2-kW fiber laser system (MSV-200W, M-SOLV) under the shielding gas of nitrogen. Different laser processing parameters including laser power, interval distance, and scanning speed were initially tried to find the optimal parameters for the subsequent detailed study. As summarized in Figure S1-S2 in the Supplementary Material, reducing interval distance and increasing laser power would result in a GNS layer with thicker hardened zone but more cracks. Therefore, a typical zigzag-path laser surface treatment parameter with a real effective laser power of 90 W, the interval distance of 0.25 mm (Figure 1), and scanning speed of 30 mm/s were selected to fabricate the crack-free GNS TiZrHfTaNb RHEA with significantly and gradually enhanced hardness along the depth direction. Prior to the microstructure characterizations and mechanical properties testing, noticeably, the laser-treated specimens were mechanically polished to achieve a relatively smooth and flat topmost surface, which could also remove the possible oxidation layer during the laser surface treatment.

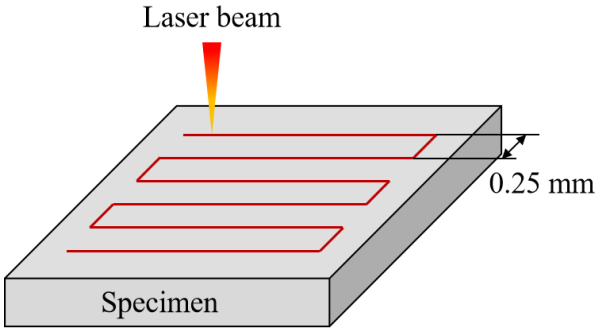

Figure 1. A schematic illustration of LSR strategy.

2.2. Microstructure characterizations

The microstructural evolution (including the grain size, compositions and phase constitutions) along the depth direction of the laser surface-treated TiZrHfTaNb RHEA was characterized by optical microscope (OM, Axio Vert. A1, ZEISS, Germany), scanning electron microscope (SEM; VEGA 3, TESCAN), plane-view HRTEM (JEOL JEM-2100F, Japan) and high-angle annular dark-field scanning TEM (HAADF-STEM) equipped with energy-dispersive X-ray spectroscopy (EDS) (FEI Technologies Inc, Hillsboro, Oregon, USA) operated at 200 kV. For the plane-view TEM observations, the specimen was first mechanically

polished from the topmost surface side to a target depth layer. Then, a ~ 25 μm-thick TEM foil was mechanically polished from the opposite side and glued to the copper ring for the single-side ion milling on the precision ion polishing system Gatan 691. Finally, the plane-view TEM observations were performed on the target depth layer from the topmost surface-side direction. In addition, X-ray diffraction (XRD) analysis was performed to identify the phases variation at different depth layers by using a Rigaku Smartlab-9 kW (Tokyo, Japan) diffractometer with Cu-Kα radiation (λ = 1.54 Å, 45 kV, 200 mA).

2.3. Hardness measurements

The Vickers microhardness along the depth direction of the laser surface-treated samples was measured using a Vickers diamond pyramidal indenter (HXD-1000TMC/LCD, Shanghai Taiming Optical Instrument Co., Ltd., Shanghai, China) under a load of 200 gf for 10 s. The hardness test at a certain depth was repeated at least 10 times to obtain the average value.

2.4. Wear tests

Dry-sliding wear tests were performed on the top surface of the laser-treated specimen using a ball-on-disk wear machine (TE99, England) at room temperature and air atmosphere. Si_3N_4 ball with a diameter of 6 mm was selected as the counterpart. Before the wear test, the surfaces of the as-cast specimens were grinded using SiC grinding papers with grit sizes down to 1200 grit to achieve a surface roughness of Sa < 0.05 μm, and the laser-treated specimens were also slightly mechanically polished to achieve a surface roughness of Sa < 0.60 μm, so as to remove the possible oxidation layer during the laser surface treatment and reserve the near top layers with nanograins. The loads of 16 N, 24 N, and 32 N were respectively adopted for the sliding wear tests with the same sliding track of 5 mm, sliding frequency of 1 Hz (sliding speed 0.01m/s), and duration of 7500 s. The sliding directions were parallel to the laser scanning directions (LD), and each reported data was the average of the three repeated tests. The values of coefficients of friction (COFs) were evaluated from their steady state of the curves. The wear rate ω was calculated based on the volume-loss equation:

$$\omega = \frac{V_{loss}}{L \times P}, \tag{1}$$

where V_{loss} is the wear volume loss (mm^3), L is the sliding distance (m), and P is the applied normal load (N), respectively. The volume below the reference surface was determined to

quantify the wear volume.

2.5. Worn surface characterizations

The surface profile and roughness of the as-cast and laser surface-treated specimens were measured by a 3D optical interferometer (ZYGO, Nexview, USA) with a height resolution of 10 nm along the Z axis. The morphology and composition of the wear tracks and debris were examined by SEM (VEGA 3, TESCAN) equipped with an EDS detector.

3. Results

3.1. Microstructural evolution of the laser-treated TiZrHfTaNb RHEA

Figure 2 shows the phase and morphology of the as-cast and laser-treated TiZrHfTaNb RHEAs. The electron backscattered diffraction (EBSD) inverse pole figure (Figure 2a) confirms that the as-cast specimen is a BCC single phase solid solution, possessing equiaxed grains with an average grain size of ~ 200 μm. Besides, bright-field TEM image and corresponding selected area electron diffraction (SAED) patterns in Figure 2(b) also reveal that there is no any other crystalline phase and/or precipitates in the BCC matrix, which is in good agreement with the XRD results in Figure 3. Figure 2(c) is an optical image for the morphology of laser-treated surface of TiZrHfTaNb RHEA, showing a good surface quality with a mean surface roughness of S_a = ~ 0.6 μm. After the laser surface treatment, the normal direction-traverse direction (ND-TD) cross-sectional optical image in Figure 2(d) also shows that a typical laser-treated zone can be clearly found along the depth direction.

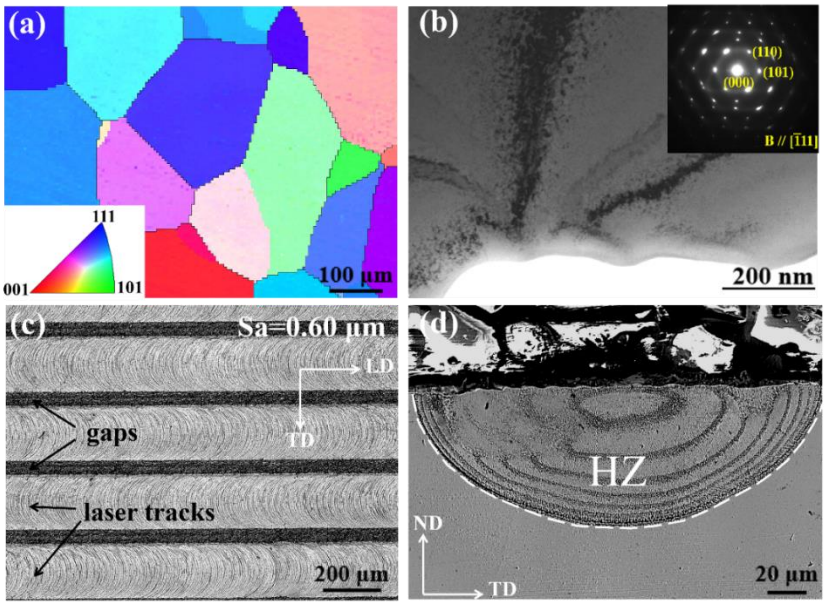

Figure 2. Phase and morphology of the as-cast and laser-treated TiZrHfTaNb RHEA. (a) EBSD inverse pole figure and (b) bright-field TEM image and corresponding SAED patterns (inset) of the as-cast TiZrHfTaNb RHEA. (c) Optical image for the morphology of laser-treated surface of TiZrHfTaNb RHEA. (d) Cross-sectional (ND-TD) SEM image of one typical surface laser-treated along the depth direction.

The cross-sectional SEM observations along the depth direction were further conducted on the laser-treated specimen, as shown in Figure 3(a-c). Specifically, Figure 3(a) indicates that a uniform HZ layer with thickness of ~ 100 μm is constructed in the topmost surface. It can be obviously found that the HZ layer has a gradient dendrite substructure with the grain size gradually increasing from the top surface to the matrix core region, according to the enlarged SEM image in Figure 3(b). The occurrence of the gradient refinement in the HZ layer should be attributed to the gradient heating and cooling along the depth direction during the laser surface treatment process. In addition, there is a special transition zone (TZ) existed between the HZ layer and the unaffected matrix, as marked by the white dashed boundary in Figure 3(a) and Figure 3(c), which might be caused by the compositional fluctuation due to the slow kinetics of homogeneous alloying of large atoms of heavier elements.[35]

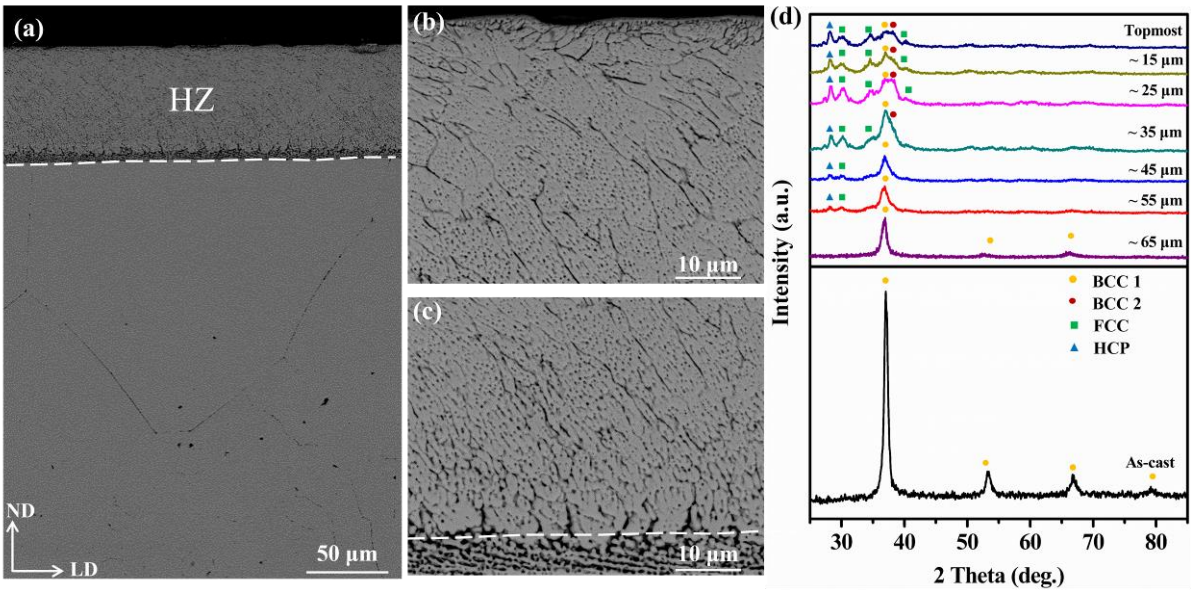

Figure 3. Morphology of the cross-section (ND-LD) of laser treated TiZrHfTaNb RHEA. (a) Low-magnification observation (the boundary profile of the hardened layer is marked in white dashed line); (b) and (c) are magnified observation of the topmost region and bottom region of HZ in (a); (d) XRD patterns of the as-cast TiZrHfTaNb RHEA and the laser treated TiZrHfTaNb RHEA at different depths.

Accordingly, Figure 3(d) gives and compares the XRD patterns of the as-cast alloy and the laser-treated alloy at different depth layers along the depth direction. Consistent with the

EBSD observation in Figure 2(a), the XRD pattern of the as-cast TiZrHfTaNb RHEA indicates a single BCC crystalline structure with the lattice constant of a = 3.345 Å (named as original BCC 1). The single BCC solid-solution phase structure maintains at the depth layer of ~ 65 μm in the laser surface-treated specimen, as shown in Figure 3(d). When the depth approaches to the top surface (*i.e.* ~ 55 μm-depth layer), new diffraction peaks can be indexed to another BCC phase (named as BCC 2) with almost equivalent lattice constant of a = 3.344 Å. In the ~ 55 μm-top surface region, noticeably, extra face-centered-cubic (FCC) and hexagonal-close-packed (HCP) phase are gradually formed once it gets closer to the top surface. Specifically, the lattice constants of the FCC and HCP phase are determined to be a_{fcc} = 4.910 Å, and a_{hcp} = 3.180 Å, c = 5.030 Å, respectively. The above results reveal that phase transitions occurred during the gradient refinement process of the TiZrHfTaNb RHEA induced by the LSR technique. Note that gradient refinement process is quite sensitive to the distribution of the heating and cooling-governed plastic strain and strain rate fields at the different depths. Therefore, detailed microstructural evolution for the grain refinement mechanism along the depth direction will be mainly dissected by the HRTEM observations at the atomic level.

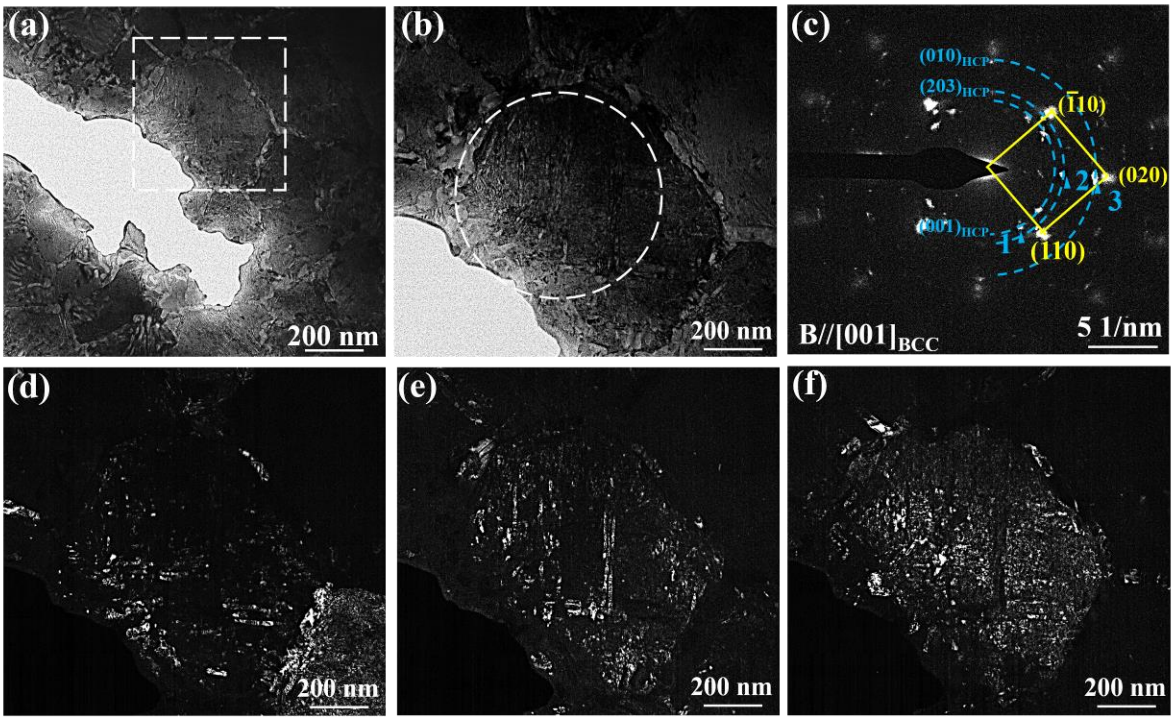

Figure 4. Microstructure of the laser treated TiZrHfTaNb RHEA at the depth of 40-60 μm below the surface. (a) bright-field TEM image, (b) the enlarged TEM image of rectangle area in (a), and (c) corresponding selected electron diffraction pattern. (d-f) Corresponding dark-field TEM images of the selected diffraction spots 1, 2 and 3 in (c), respectively.

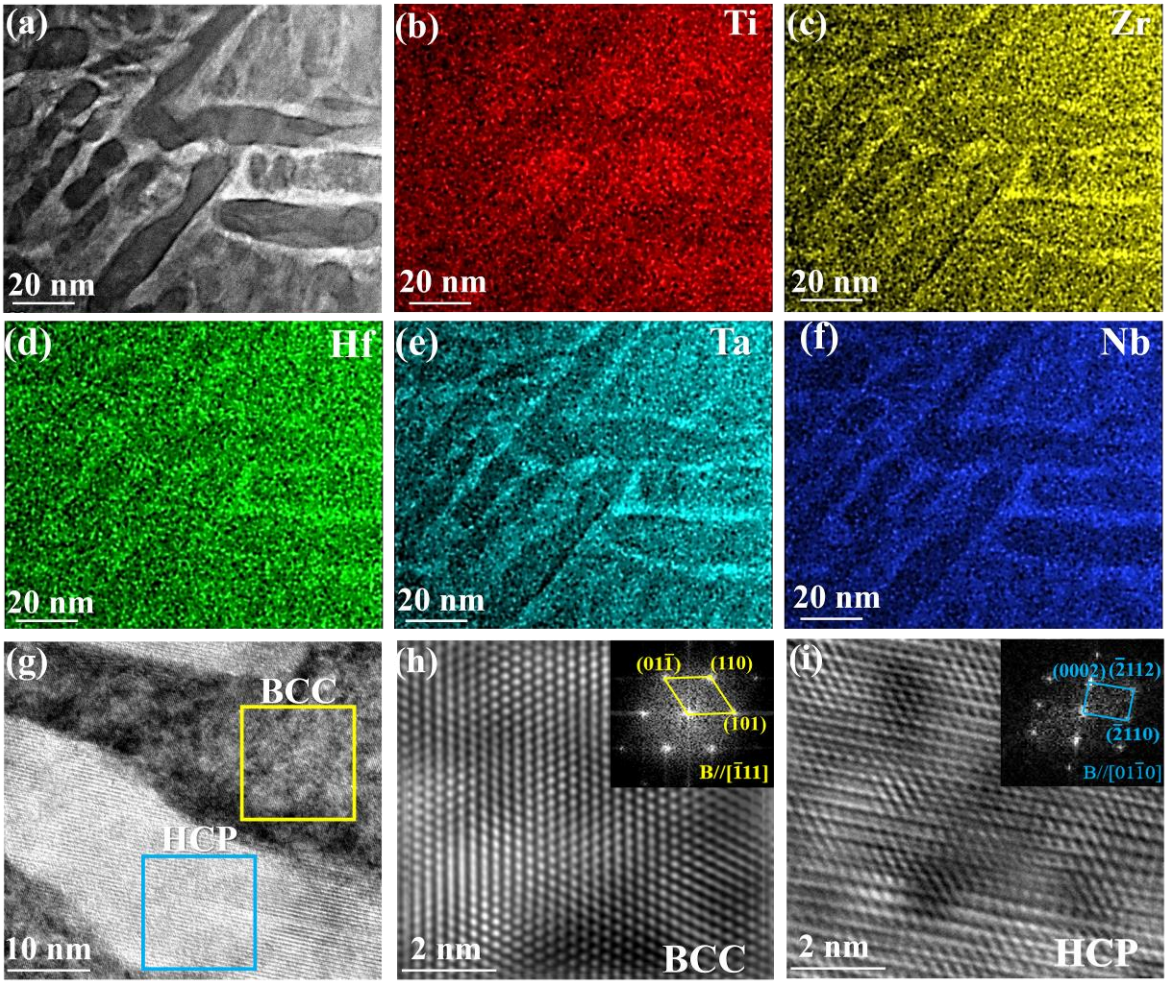

Figure 5. Phase and composition characterization at the depth of 40-60 μm below the surface. (a) HAADF-STEM image of secondary phase. (b-f) EDS elemental maps of Ti, Zr, Hf, Ta, and Nb, respectively. (g) HRTEM image obtained at the interface of the BCC matrix and HCP grains. (h-i) atomic Fourier-filtered images enraged from the squares marked in (g) and corresponding fast Fourier transform (FFT) patterns (insets), respectively.

Several representative TEM images at the depth ranging 40-60 μm below the surface of the laser-treated TiZrHfTaNb RHEA are firstly given in Figure 4. In contrast to the original as-cast grain size of ~ 200 μm, Figure 4(a-b) indicates that the grain size of the laser-treated TiZrHfTaNb RHEA at this depth layer is significantly refined to ~ 300 nm. In addition, some bright rod-like precipitates were located in both interior and GBs of these refined equiaxed BCC grains. Figure 4(d-f) gives the corresponding dark-field TEM images of the selected diffraction spots 1, 2 and 3 in Figure 4(c), respectively, showing the rod-like precipitates from three different orientations. Therefore, HAADF-STEM image (Figure 5(a)) with EDS elemental maps (Figure 5(b-f)) and HRTEM images (Figure 5(g-i)) are provided to further

identify the compositions and the crystalline structures of these rod-like precipitates (Figure 5). The HAADF-STEM image (Figure 5(a)) and the corresponding EDS elemental maps (Figure 5(b-f)) show that the precipitates are rich in Zr and Hf. HRTEM analysis (Figure 5(g-i)) reveals that the bright rod-like precipitate is an HfZr-rich HCP phase. The lattice constants of HCP and BCC matrix phases are measured to be a_{hcp} = ~ 3.18 Å, c = ~ 5.03 Å, and a_{bcc} = ~ 3.34 Å, consistent with the results based on the XRD analysis.

Table 1. Quantitative EDS analysis of the region shown in Figure 5(a).

Location of analysis	Element (at. %)				
	Ti	Zr	Hf	Ta	Nb
Precipitates	17.4 ± 1.4	24.6 ± 2.2	24.4 ± 2.3	16.8 ± 1.4	16.8 ± 1.4
Phase boundary	19.8 ± 1.7	15.6 ± 1.2	12.6 ± 1.0	27.2 ± 2.3	24.8 ± 2.1
Matrix	20.3 ± 1.9	19.9 ± 1.7	19.8 ± 1.3	20.4 ± 1.6	19.6 ± 1.9

The TEM image (Figure 6a) in the depth ranging 30-40 μm below the surface of the laser-treated specimen shows the finer grains with typical manifold structure [42]. The grains consist of irregularly shaped aggregates or chains connected to each other and thus form the continuous networks. The corresponding SAED pattern (Figure 6(b)) shows the presence of another FCC phase in addition to the pre-transformed HfZr-rich HCP phase and matrix BCC phase, suggesting the phase transformation at this depth layer. Therefore, HRTEM image (Figure 6(c)) and corresponding FFT pattern (Figure 6(d)) are analyzed and revealed that the lattice constant of these FCC precipitates is measured to be a = ~ 4.90 Å, in good agreement with the result calculated from XRD. The lattice constants of the pre-transformed HfZr-rich HCP phase and matrix BCC phase remain unchanged. Particularly, an atomic Fourier-filtered image of the region containing FCC precipitate, HCP precipitate and the BCC matrix reveals the typical orientation relationship, following $[001]_{BCC}//[001]_{FCC}//[2\bar{1}\bar{1}0]_{HCP}$ and $(010)_{BCC}//(020)_{FCC}//(01\bar{1}0)_{HCP}$. Note that the misfit interplanar spacing δ in this orientation relationship between BCC-FCC, BCC-HCP and HCP-FCC are calculated as small as 3.74%, 4.75%, and 2.62%, respectively. Therefore, the coherent interfacial structures can be formed between FCC, HCP and BCC phases,[43] as shown in Figure 6(e).

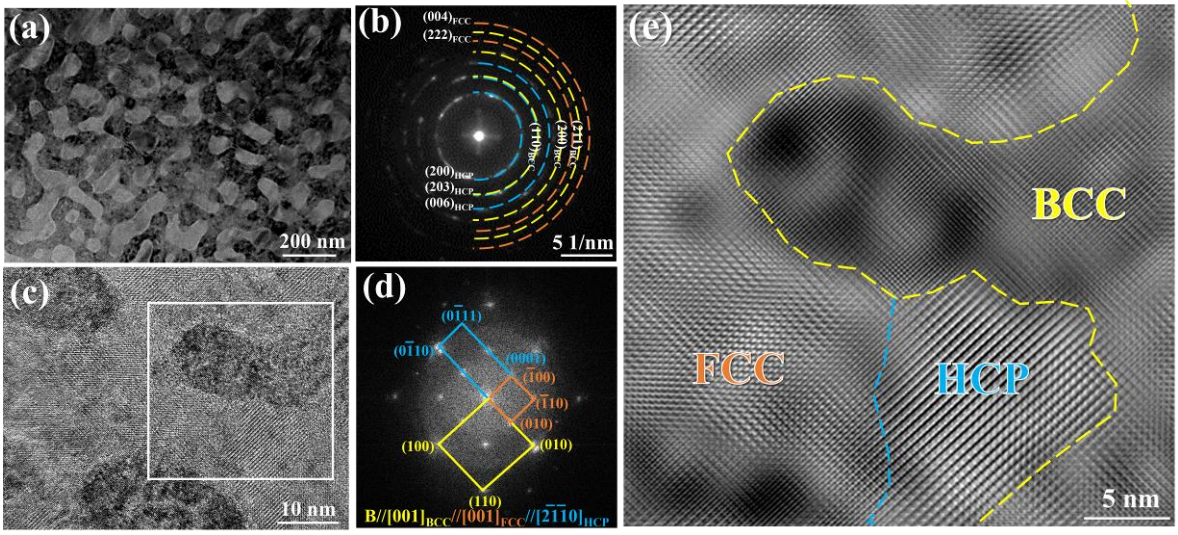

Figure 6. TEM characterization of the region at the depth of 30-40 μm below the surface. (a) Bright-field TEM image and (b) corresponding SAED pattern. (c) HRTEM image of a representative region containing BCC, FCC and HCP phases. (d-e) FFT pattern and enlarged inverse FFT image of the square area marked in (c).

The microstructure in depth of 20-30 μm below the surface (Figure 7) shows the continuous grain refinement when approaching the top surface of the laser-treated TiZrHfTaNb RHEA. The grain size is refined to be ~ 55 nm in the depth of 20-30 μm (Figure 7(c)) and further refined to ~ 35 nm in the depth of 10-20 μm (Figure S3). The grains in this region (Figure 7d) show four primary contrasts, *i.e.*, dark (grain 1), gray (grain 2), light gray (grain 3) and light (grain 4), respectively, which are TiNb-rich phase, ZrHf- rich phase, TiZrHf-rich phase and TaNb-rich phase, respectively, based on quantitative EDS analysis (Table 2). HRTEM (Figure 7(j)), inverse FFT (Figure 7(k)), and atomic Fourier-filtered (Figure 7(l)) images reveal that the ZrHf-rich phase, TiZrHf-rich phase and TiNb-rich phase are HCP phase (a = ~ 3.18 Å, c = ~ 5.03 Å), FCC phase (a = ~ 4.90 Å) and BCC 1 phase (a = ~ 3.34 Å), respectively. While, the TaNb-rich phase can also be determined to be BCC 2 phase with the lattice constant of ~3.35Å, consistent with the result in literature.[34] Obviously, complex phase decomposition was induced during the formation of GNS TiZrHfTaNb RHEA HZ layer by laser surface treatment.

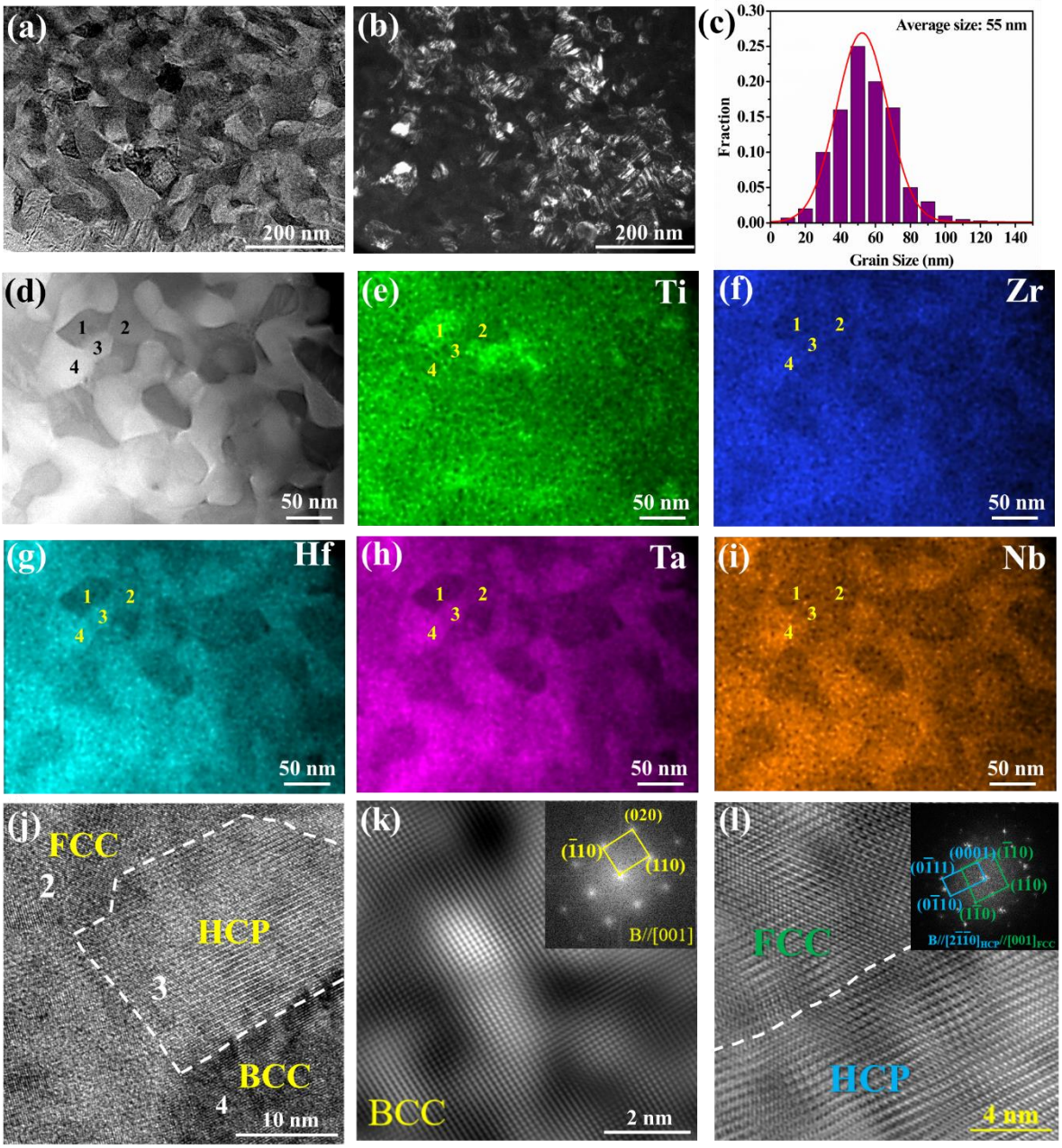

Figure 7. Microstructure of the laser treated TiZrHfTaNb RHEA at the depth of 20-30 μm below the surface. (a) Bright-field TEM image at the depth of 20-30 μm, and corresponding (b-c) dark-field TEM image and grain size distribution; (d) HADDF-STEM image; (e-i) corresponding EDS elemental maps of Ti, Zr, Hf, Ta, and Nb, respectively. (j) HRTEM image of the including grains 2, 3 and 4. (k-l) IFFT and corresponding FFT (insets) images of the BCC grain (grain 4), and neighboring FCC - HCP grains (gain 3 and 4) in (j), respectively.

Table 2. Quantitative EDS analysis for the areas marked in Figure 7d.

Location of analysis	Crystal structure	Element (at. %)				
		Ti	Zr	Hf	Ta	Nb
1	BCC 1	44.9 ± 3.5	13.9 ± 1.1	8.8 ± 1.1	13.9 ± 1.3	18.5 ± 1.3

2	HCP	17.9 ± 1.6	26.2 ± 2.1	26.1 ± 2.3	15.1 ± 1.3	14.7 ±1.4
3	FCC	25.0 ± 2.1	24.7 ± 2.2	23.4 ± 2.3	13.1 ± 1.3	13.8 ± 1.4
4	BCC 2	16.1 ± 1.3	12.8 ± 1.0	10.9 ± 1.1	29.9 ± 2.5	30.3 ± 2.8

Finally, it is interesting to find that the grain size near the topmost surface of laser-treated TiZrHfTaNb RHEA is dramatically refined down to only several nanometers (Figure 8(a-c)). The average size of NGs in the surface is determined to be ~ 8 nm (Figure 8(c)), which is the smallest record in the reported HEAs by SPD. Figure 8(b) indicates that these extremely refined NGs are severely distorted, even demonstrating relatively ambiguous GBs. Moreover, HRTEM images and corresponding atomic Fourier-filtered images (Figure 8(d-f)) show that severe lattice distortion and some dislocations in the interior of the BCC matrix NGs. While, a high density of partial dislocations and deformation nanotwins are found to across the FCC NGs (Figure 8(f)), due to the different dislocation slip systems in FCC structure.

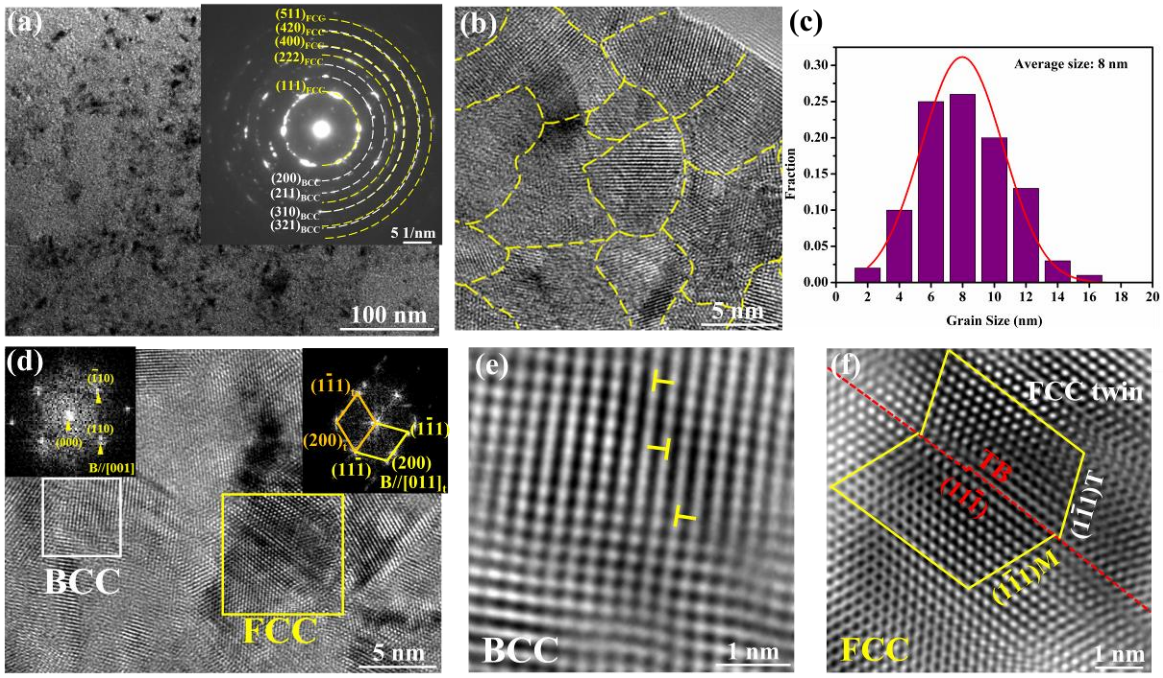

Figure 8. Microstructure of the laser treated TiZrHfTaNb RHEA near the topmost surface (< 10 μm). (a) TEM image with corresponding SAED pattern. (b) HRTEM image showing the NGs with extremely small grain size and (c) grain size distribution. (d) HRTEM image of the BCC and FCC NGs. (e-f) Atomic Fourier-filtered images of the BCC and FCC NGs showing the different crystalline defects.

3.2 Surface hardness and tribological performance

3.2.1 Microhardness variation along the depth direction

Based on the detailed characterizations of the microstructural evolution along the depth direction from the matrix to the topmost surface, it can be concluded that a GNS layer with a thickness of ~ 100 μm has been introduced into bulk TiZrHfTaNb RHEA by the laser surface treatment. Therefore, this GNS layer is expected to have the enhanced mechanical properties, especially the surface hardness and wear performance. First, the dependence of microhardness on depth was measured along the cross-sectional (ND-LD) direction of the laser-treated specimen. As shown in Figure 9(a), the microhardness in the topmost surface reaches a maximum value of ~ 650 HV, which is gradually decreased to the value of ~ 240 HV in the matrix at a depth of ~ 100 μm, denoting a significant increment in the surface by a factor of ~ 2.7. In addition, a plot of the grain size versus the depth away from the surface (Figure 9(a)) clearly shows that the grain size is gradually decreased from the original ~ 200 μm in the matrix to ~ 8 nm in the topmost surface.

Through constructing a Hall-Petch plot, Figure 9(b) further displays the significantly enhanced strength as a function of grain size for the laser-treated GNS TiZrHfTaNb RHEA, comparing with some experimental results of the refined HEAs from literature [7, 8, 19, 20, 29, 30, 34, 44-50]. Note that the conversion between hardness values (HV) and yield strength (σ_y) can be estimated according to the empirical relation: $0.3\sigma_y \approx$ HV [51]. Apparently, the record for the smallest grain size of ~ 8 nm with the highest yield strength of ~ 2.15 GPa is achieved in our work in the topmost surface of the laser-treated TiZrHfTaNb RHEA. The strengthening-softening transition with negative Hall-Petch relationship has been widely reported for various nanostructured metals, once their grain sizes are refined to below some critical values (normally < ~ 20-30 nm) [29, 30]. In contrast, the extremely refined grain size in our work overcomes the strengthening-softening transition. Nonetheless, the Hall-Petch slope becomes lower from the grain size of ~ 150 nm in the depth layer of ~ 50 μm to the topmost surface. It implies the different grain refinement and corresponding strengthening mechanisms when more approaching to the surface of the laser-treated specimen. According to the above microstructure characterizations, nano-sized FCC and HCP phases with more dislocation slip systems start to decompose from the BCC matrix with the average grain size of ~ 150 nm in the depth layer of ~ 40 μm in the GNS layer, which might contribute to the cooperative strengthening effect for maintaining a positive Hall-Petch slope with a lower value in the small-

grain size region. Relative to the reference data, it is evident that the laser surface treatment-introduced GNS TiZrHfTaNb RHEA in this work could dramatically enhance the surface hardness without softening effect, thus may further potentially improve the correlated tribological performance.

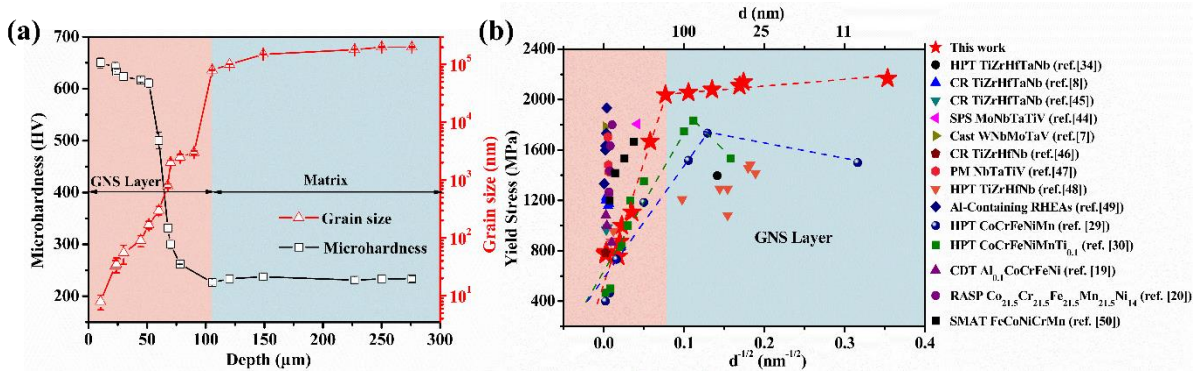

Figure 9. (a) Grain size and microhardness varying along the depth away from the surface of the laser treated TiZrHfTaNb RHEA. (b) A Hall-Petch plot of calculated yield stress for GNS TiZrHfTaNb RHEA in this work comparing with that of cold rolled (CR) TiZrHfTaNb (ref. [8] and ref. [45]), HPT-processed TiZrHfTaNb (ref. [34]), spark-plasma-sintered (SPS) MoNbTaTiV (ref. [44]), cast WNbMoTaV (ref. [7]), CR TiZrHfNb (ref. [46]), powder metallurgy (PM) NbTaTiV (ref. [47]), HPT TiZrHfNb (ref. [48]), Al-containing RHEAs (ref. [49]), HPT-processed CoCrFeNiMn (ref. [29]) and CoCrFeNiMnTi0.1 (ref. [30]), cyclic dynamic torsion (CTD) processed $Al_{0.1}$CoCrFeNi (ref. [19]), rotationally accelerated shot peening (RASP) treated $Co_{21.5}Cr_{21.5}Fe_{21.5}Mn_{21.5}Ni_{14}$ (ref. [20]), and surface mechanical attrition treated (SMAT) FeCoNiCrMn (ref. [50]).

3.2.2 Friction and wear performance

Sliding wear is a key factor that limits the lifetime of metallic components for a wide range of functional and structural applications [52]. Thus, the tribological properties of the laser-treated GNS TiZrHfTaNb RHEA were investigated systematically with the as-cast specimen as control. The variations in COFs as a function of sliding distance for the as-cast and laser-treated specimens are presented in Figure 10(a). The sliding velocity keeps 0.01 m/s under three different normal loads increasing from 16 N to 32 N. It shows that each wear reaches the steady state after an initial running-in period of ~ 2000 s. The corresponding data at the steady state are summarized in Table 3. Upon the different loads, the mean COFs of the two specimens keep no apparent change, *i.e*. ranging from 0.29 to 0.30 (as-cast specimen) and 0.32 to 0.34 (laser-treated specimen), respectively. No obvious reduction in COFs of the laser-treated GNS TiZrHfTaNb RHEA are revealed.

The wear track profile can be firstly integrated to obtain the average cross-sectional area

(Figure 10(c-d)). The wear volume loss was calculated by multiplying the average track cross-sectional area and track length. The calculated wear rates were summarized in Figure 10(b) and Table 3. The representative surface profile of the wear tracks of the laser-treated alloy under 24 N (Figure 10(d)) shows the width of ~ 800 μm and maximum depth of ~ 3.5 μm, which are apparently lower than those of as-cast alloy (Figure 10(c)) under the same wear conditions. The average wear rate of the as-cast alloy is calculated to slightly increase from 3.41×10^{-5} to 3.83×10^{-5} $mm^3/m\cdot N$ under the loads from 16 N to 32 N (Figure 10(b)). Noticeably, the corresponding values of the laser-treated alloy are in the range of 2.21×10^{-6} to 2.94×10^{-6} $mm^3/m\cdot N$, exhibiting a markedly reduction in wear rate by an order of magnitude. In addition, although the laser-treated specimens have the higher original surface roughness, the worn surfaces of laser-treated specimens are relatively smoother with the lower surface roughness S_a (Figure 10(f)) than those of as-cast specimens (Figure 10(e)), showing an promoted worn surface quality after the laser surface treatment, as also summarized in Table 3. The results of the wear rate, wear volume loss, and surface roughness are consistently to indicate the exceptional wear resistance of the laser-treated TiZrHfTaNb RHEAs.

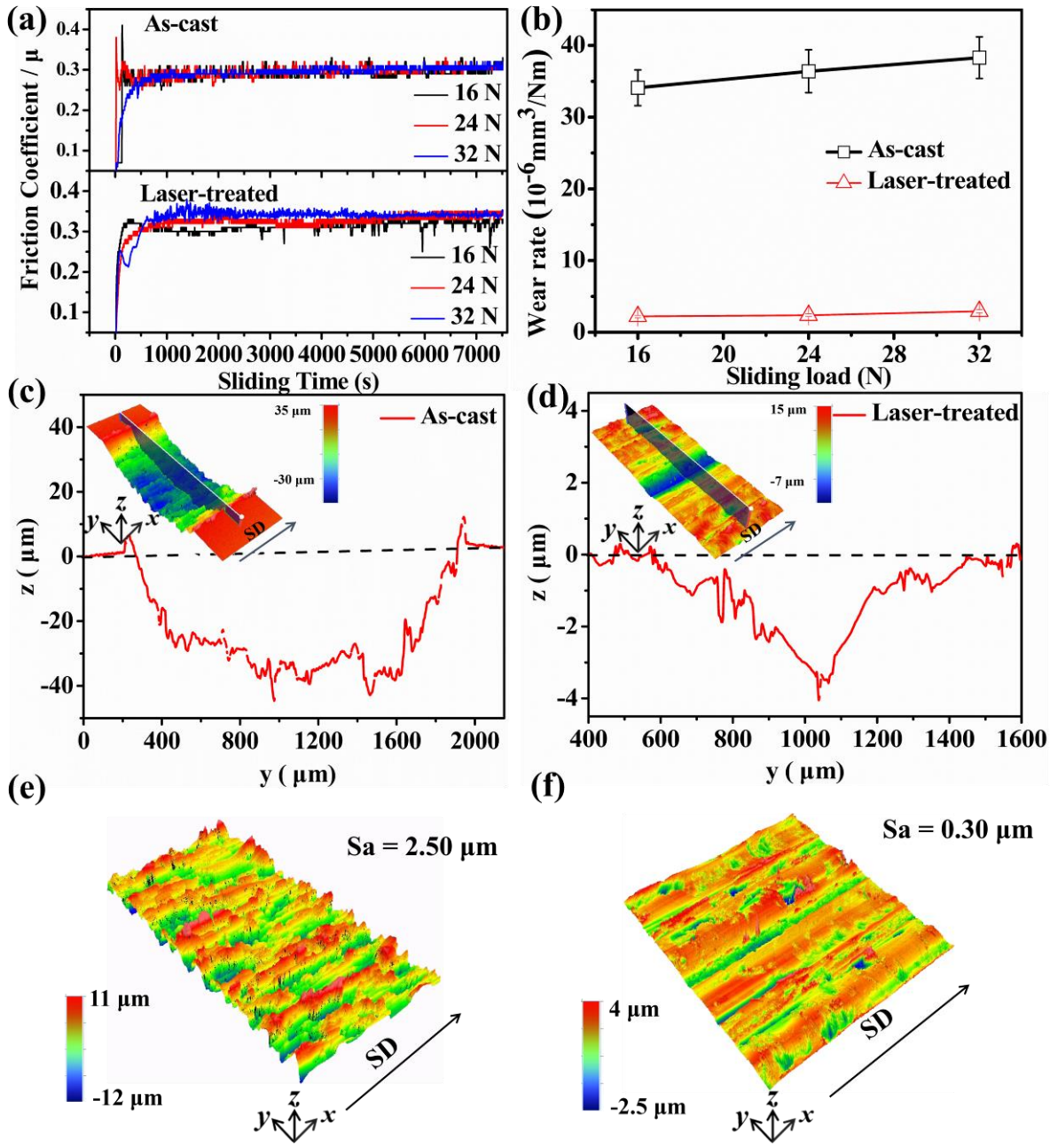

Figure 10. Comparisons of dry-sliding wear performance between the laser surface treated and as-cast TiZrHfTaNb RHEA. (a) The COFs as a function of sliding time of as-cast and laser-treated specimens under different normal loads (16 N, 24 N and 32 N). (b) The wear rates of as-cast and laser-treated specimens under different normal loads (16 N, 24 N and 32 N). (c) and (d) showing 2D cross-sectional profile along the dotted line (y direction, TD) in the corresponding inset. The insets in (c) and (d) display the 3D profile of wear tracks of as-cast and laser-treated specimens under the normal load of 24 N, respectively. (e) and (f) are 3D profiles of worn surface for as-cast alloy and laser-treated alloy under the normal load of 24 N, respectively.

Table 3 Wear characteristics of the alloys upon dry sliding against Si_3N_4 at room temperature.

Specimen	Normal load	COFs	Wear rate (mm^3/m·N)	Wear track roughness /Sa

	(N)			(μm)
As-cast	16	0.29 ± 0.01	3.41 (± 0.25) ×10^{-5}	1.90 ± 0.15
	24	0.30 ± 0.01	3.64 (± 0.30) ×10^{-5}	1.97 ± 0.16
	32	0.30 ± 0.01	3.83 (± 0.29) ×10^{-5}	2.46 ± 0.19
Laser-treated	16	0.32 ± 0.02	2.21 (± 0.17) ×10^{-6}	0.18 ± 0.07
	24	0.33 ± 0.01	2.38 (± 0.20) ×10^{-6}	0.47 ± 0.17
	32	0.34 ± 0.02	2.94 (± 0.22) ×10^{-6}	0.84 ± 0.20

In addition, wear surface morphology and composition, including the wear tracks and debris, of the as-cast and laser-treated TiZrHfTaNb RHEAs were characterized and compared (Figure 11) for further insight into the wear mechanism. Typical characteristics of abrasive wear that consists of narrow plowing grooves along the sliding direction with a few micro-cracks are both observed in as-cast and laser-treated TiZrHfTaNb RHEAs, as shown in Figures 11(a-b) and (d-e). The grooves on the laser-treated alloys are much shallower (Figure 11(b)) than those on the as-cast alloys (Figure 11(e)), indicating that the abrasive wear mechanism has been greatly alleviated after LSR. Besides, oxide layers were confirmed to form on the worn surfaces of the two alloys (Figure 11(b) and (e)), according to the EDS mapping analysis (Figure 11(c) and (f)), indicating the occurrence of oxidation wear mechanism. However, the oxide layers on the laser-treated specimens are mainly composed of silicon oxide (Figure 11(f)), while the oxides on the as-cast specimens are the mixtures of metal and silicon oxide (Figure 11(c)). Moreover, EDS analysis of wear debris (Figure S4) also shows that both the compositions of the ball and disk are detected in the wear debris, *i.e.* gray fine particles are from the Si_3N_4 counter ball while bright coarse particles are referred to the TiZrHfTaNb HEA disk, which suggests the adhesive wear behavior. The results indicate that the mixed wear mechanisms including abrasive wear, oxidation wear and adhesive wear occur in both specimens. Nonetheless, deeper grooves, rougher oxide layer, and more wear debris are obviously observed for the as-cast alloys, indicating a much severer wear in comparison with the laser-treated alloys.

For further clarifying the effects of the relative position of the sliding direction - laser scanning path on the wear performance of the laser-treated specimens, the tribological properties of the laser-treated specimen in the sliding directions perpendicular to the laser

scanning direction were also evaluated. The corresponding results are summarized in Figure S5-S6 and Table S1 in the Supplementary Material. It is found that, under different sliding directions, there are no significant differences in the wear performance, including the values of COFs, wear rate, wear track roughness, the surface morphology as well as the compositional characteristics. Thus, it can be confirmed that the relative position of sliding direction - laser scanning direction has almost no effect on the wear performance of the laser-treated specimens, as all the wear behaviors occur in the uniform GNS layer of the specimens with the depth of wear region less than 10 μm.

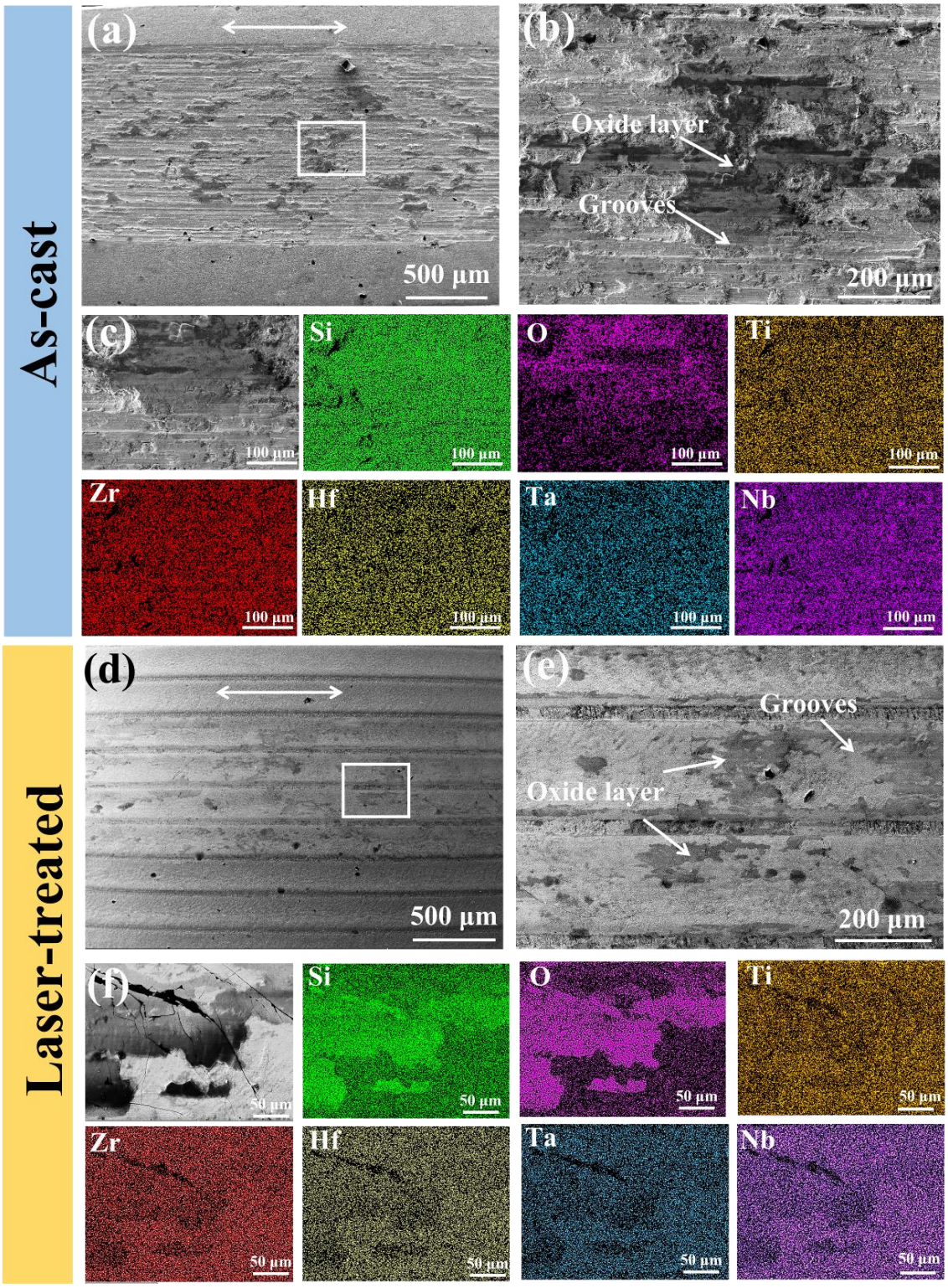

Figure 11. Surface morphology and composition of the alloys after dry sliding against Si_3N_4 under 24 N at room temperature. (a) and (d) are SEM images of the worn surfaces of as-cast alloy and laser-treated alloy, respectively; The arrows indicate the sliding directions; (b) and (e) are high-magnification SEM images of the selected region in (a) and (d), respectively; (c) and (f) are EDS elemental maps of the worn surfaces of as-cast alloy and laser-treated alloy, respectively.

4. Discussion

4.1 Phase decomposition-mediated gradient refinement process

Our microstructural characterization results reveal the phase decomposition-mediated gradient refinement process of GNS TiZrHfTaNb RHEA by laser surface treatment technique. The original BCC phase was gradually decomposed into several distinct phases, *i.e.* TiNb- and TaNb-rich BCC phases, ZrHf-rich HCP phase, and TiZrHf-rich FCC phase, along the depth direction. The phase decomposition phenomenon in TiZrHfTaNb RHEA was also reported in other literature. For example, Schuh *et al.*[34], reported that the phase decomposition of the lattice constants of BCC and HCP phases were determined as a_{bcc} = ~3.350 Å and a_{hcp} = 3.198 Å, c = ~ 5.070 Å, respectively, equivalent to the values in the present work. Yang *et al.*[53] also observed the phase decomposition in the annealed TiZrHfTaNb RHEA alloy, *i.e.* decomposition into ZrHf-rich HCP phase after annealing at 1000 ℃ for 24 h while two TiZrHf-rich FCC phases after annealing at 1450 ℃ for 1 week. In addition, the TaNb-rich second-phase particles were also observed in the cold-rolled TiZrHfNbTa RHEA after annealing at 800 °C [54].

Apparently, the composition segregation and gradient refinement of the decomposed phases should be related to the characteristics of the TiZrHfTaNb RHEA and the processes of heating and cooling during the laser surface treatment. On one hand, it has been suggested that the occurrence of the composition-segregation phase decomposition in TiZrNbHfTa RHEA might be attributed to the difference in the Gibbs free energies between different phases and kinetics properties of refectory elements. For example, the growth of the TaNb-rich BCC particles could facilitate in eliminating crystalline defects and lowering the total free energy [54]. The sluggish nucleation and growth of the TaNb-enriched particles are likely due to the slow diffusion of Nb and Ta atoms with the highest melting points [54-56]. While, the formation of the ZrHf-rich HCP as well as TiZrHf-rich FCC phases in this work can be explained by the fact that metastable phases usually form in different regions depending on the composition [57]. On the other hand, laser surface treatment-induced severe plastic strain and temperature fields and their gradient distributions along the depth direction further contribute to the phase decomposition-mediated gradient refinement process. More specifically, the

highest temperature can be achieved by the highest heating rate in the topmost surface of the specimen during the LSR process, which provides the highest possibility for the nucleation of new phases. However, the surface layer has the highest cooling rate. The whole cooling process might be lasted only tens of milliseconds during the LSR process [58]. Such a short time could not allow nano-sized nuclei of the newly formed phases to grow up to a large size, due to relatively slow diffusion kinetics in the solid-state, especially for the refectory elements in the present work. Hence, the grain size can be even refined to several nanometers in the surface layer, as the TEM results shown in Figure 8. In addition, the nanostructuring process is considered to benefit the phase decomposition, due to the faster diffusion pathways and possible more nucleation sites of the nanostructure with significantly enhanced density of interfaces/boundaries[34]. In consequence, the gradient distributed plastic strain and temperature fields during the laser surface treatment lead to the multi-phase GNS TiZrNbHfTa RHEA layer in our work. Additionally, grain refinement degree in the surface layer mainly depends on the cooling rate during LSR. Generally, the temperature gradient gradually increases along the depth direction towards the top surface during LSR, resulting in a gradient cool rate along the depth direction. Lower cool rate in the deeper depth allows a nano-sized nucleus to grow to a larger size. Consequently, the average grain size is increased with an increase in the distance away from the surface.

Based on the above results and analysis, the microstructural evolution and phase decomposition/transformation governing the gradient refinement mechanisms for the formation of GNS TiZrHfTaNb RHEA layer processed by LSR technique can be schematically summarized in Figure 12. When the depth is larger than ~100 μm below the laser-treated surface, there are only few dislocations existed inside of the unaffected matrix CG TiZrHfTaNb with single BCC structure (see Figure 12(a)). Figure 12(b) shows that ZrHf-rich HCP phase is started to form in the interior and GBs of the BCC grains in the depth of ~60 μm, denoting the average grain of hundreds of nanometers and a phase transformation of BCC → HCP. It has been reported that BCC → HCP phase transformation configuration in metastable titanium alloy can be greatly affected by the BCC/HCP stabilizer competition [59], in which both the elements of Zr and Hf can work as the HCP stabilizers. Similarly, the segregation of Zr and Hf in the HCP phase during the current laser surface treatment would result in the corresponding

component approaching the critical line of HCP formation, thus leading to the BCC → HCP phase transformation. In the depth ranging 30-40 μm, TiZrHf-rich FCC structured phases are transited to connect with HCP and BCC phases, forming a continuous network-like structure shown in Figure 12(c). With the increase of the plastic strain and temperature fields, these grains are further refined to tens of nanometers in the depth of 10-30 μm, as shown in Figure 12(d). Due to the similar chemical composition, it should be noted that the ZrHf-rich HCP could be easily transformed to the TiZrHf-rich FCC phase (see Table 2). Besides, the coherent interfacial structures between the two phases following $[001]_{FCC}//[2\bar{1}\bar{1}0]_{HCP}$ and $(020)_{FCC}//(01\bar{1}0)_{HCP}$ (see Figure 6-7) is also favorable for the phase transformation of HCP → FCC without large lattice distortion. Therefore, the phase transformation/decomposition during the laser surface treatment of TiZrHfTaNb RHEAs is followed by the sequence of BCC → HCP → FCC. Finally, Figure 12(e) depicts that the average grain size is refined to only ~ 8 nm in the topmost surface of the laser-treated specimen.

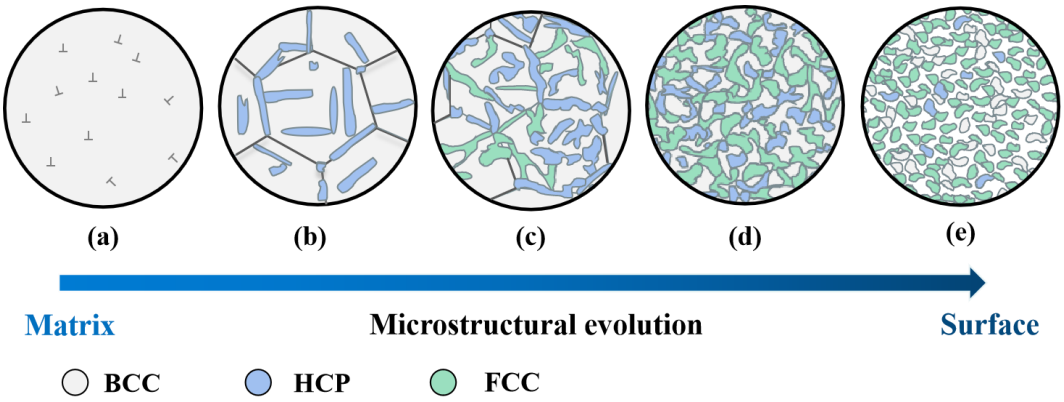

Figure 12. Schematic diagram of microstructural evolution processes of TiZrHfTaNb RHEA induced by LSR. (a) Coarse BCC grain with multiple dislocations inside; (b) grains get refined, and HCP structured phases occur in the interior and grain boundaries of BCC grains; (c) FCC structured phases occur and grains get further refined, forming continuous network-like microstructures; (d) grains are continually refined and get disconnected; (e) grains are final refined to several nanometers.

4.2 GNS RHEA with significantly enhanced wear resistance

Studies on wear behaviors of RHEAs are critical in evaluating their application merits. Numerous works have been conducted to evaluate the wear resistance of RHEAs, most of which have shown superior wear resistance in comparison with some conventional alloys [60-64]. Table 4 summarizes the wear characteristics of some RHEAs reported in recent years.

Notably, the laser-treated TiZrHfTaNb RHEA in this work show the wear rates with the order of 10^{-6} mm^3 /(N·m), obviously lower than that of as-cast counterpart with the order of 10^{-5} mm^3 /(N·m) and other referenced RHEAs with the order of 10^{-1}-10^{-4} mm^3 /(N·m), showing the excellent wear resistance after laser surface treatment.

Table 4. Wear performance comparison between TiZrHfTaNb RHEA in this work and other RHEAs from reported literature.

Specimen	Wear condition			COFs	Wear rate (mm3 /(N·m))	Ref.
	Counter-body	Normal load (N)	Sliding speed (m/s)			
Laser-treated TiZrHfTaNb	6 mm Si_3N_4	16, 24, 32	0.01	0.32-0.34	(2.21-2.94) $\times10^{-6}$	This work
As-cast TiZrHfTaNb				0.29-0.30	(3.41-3.83) $\times10^{-5}$	
723 K-annealed TiZrHfTaNb	6 mm Si_3N_4	5	0.035, 0.35	0.46-0.65	(0.5-2.5) $\times10^{-4}$	[60]
723 K-annealed TiZrHfNb	6 mm Si_3N_4	5	0.035, 0.35	0.42-0.62	(1.7-2.2) $\times10^{-4}$	[60]
As-cast MoNbTaVW	6 mm Al_2O_3 6 mm $100Cr_6$	5	0.1	~ 0.5 ~ 0.7	0.83 0.21-0.23	[61]
As-cast MoNbTaTiZr	6 mm Al_2O_3 6 mm $100Cr_6$	5	0.1	~0.72 ~ 0.6	0.13 1.5×10^{-2}	[62]
730 K-annealed HfTaTiVZr	3 mm Si_3N_4	50	0.035	~0.25	~ 10^{-4}	[63]
730 K-annealed TaTiVWZr				~0.32	~ 10^{-4}	
1200 ℃-annealed HfNbTiZr	600 nm 90° Cone-spherical diamond tip (Nanoscratch)	0.01-1	(0.01, 0.1, 1) $\times10^{-6}$	~ 0.16	1.28×10^{-2}	[64]

In addition to the wear rate, the results in this work indicate that the wear volume loss and surface roughness are also markedly improved in the laser surface treatment-introduced GNS TiZrHfTaNb RHEA. On one hand, the introduction of a GNS surface layer has been proved to be effective in enhancing wear performance, as reported in the past decades.[26, 65] Note that wear resistance is empirically correlated with the hardness of the metals, it is therefore expected that the hardened homogeneous NGs metals and alloys with the strengthening effect of grain size reduction should have the better wear resistance. Due to the suppressed dislocation activities, however, the ductility is significantly sacrificed in homogeneous NGs metals, resulting in no improvement in wear performance [12]. Alternatively, the GNS metals can harvest the strength-ductility synergy based on the cooperation of the strain/stress partitioning along the gradient direction, which can effectively suppress the strain localization to achieve a

large uniform plastic deformation. Therefore, the crack initiation and propagation correlated to the surface roughening and delaminating can be delayed in the GNS metals [66, 67], contributing to the improvement of wear resistance. The EDS analysis (Figure 11(c) and (f)) in this work also confirms this effect. The plowing grooves on the laser-treated alloys are much shallower (Figure 11(b)) than those on the as-cast alloys (Figure 11(e)). Noticeably, the effectively refined GNS TiZrHfTaNb RHEA can significantly enhance the hardness/strength along the depth direction, especially showing the hardness of ~ 650 HV (strength of ~ 2.15 GPa) at the topmost surface layer with an average grain size of only ~ 8 nm, as shown in Figure 9. Such ultra-high surface hardness can greatly delay the detachment in the LSR-induced GNS disk during the sliding process. In contrast, the Si_3N_4 counter-body material is more prone to detach during the wear comparing with the laser-treated disk material. As a result, the detached Si_3N_4 debris are subsequently compacted, oxidized and finally formed an almost simplex compact silicon oxide layer on the worn laser-treated specimens (Figure 11(f)), rather than the mixtures of metal oxides and partial silicon oxides on the worn as-cast specimens (Figure 11(c)). The dense silicon oxide layer formed during the wear can shield the specimen from damage, thus better enhancing the wear resistance [68]. However, the silicon oxide layer with strong covalent bonds make themselves very hard and difficult to shear on the sliding surface, thus inducing higher shear stress during the sliding friction comparing with the mixed oxide layer on the sliding as-cast counterpart [69, 70]. Therefore, it might be the factor responsible for the no improvement in the COFs after the laser surface treatment in the present work, *i.e.* slightly increasing from original 0.29-0.30 in as-cast specimens to 0.32-0.34 in laser-treated counterparts, as shown in Figure 10.

On the other hand, the decomposition-induced nanoscale precipitates are also beneficial to enhance the wear resistance of the laser surface treatment-introduced GNS TiZrHfTaNb HEA. The presence of the nanoparticles usually acts as the obstacles that impede dislocations motion and further hinder the violent plastic flow of the matrix, which therefore leads to a small deformation depth during the sliding wear. Noticeably, the decomposed HCP and FCC nanoparticles have more dislocation slip systems in comparison with the BCC matrix. In this regard, the nucleation and motion of dislocation activities in HCP and FCC can be still activated to contribute to the plasticity, if needed, as the dislocations and deformation

nanotwins observed in Figure 8. Based on the above discussion, the significant improvement in wear resistance for the TiZrHfTaNb RHEA in the present work is attributed to the cooperatively effects of the decomposed multi-phase and GNS layer by laser surface treatment.

5. Conclusions

In this work, a GNS layer on bulk TiZrHfTaNb RHEA was fabricated by a facile LSR-based surface treatment technique. The microstructural evolution of the GNS layer was dissected along the depth direction from the matrix region to the topmost surface and the wear performance of laser-treated specimen was also evaluated in comparison with the as-cast alloys. The key findings are summarized as follows:

(1) LSR-based surface treated CG TiZrHfTaNb RHEA results in a significant grain refinement and the formation of GNS layer with a thickness of ~ 100 μm. The average grain size is dramatically refined from the original ~ 200 μm to ~ 8 nm upon approaching the surface.

(2) Due to the plastic strain and temperature fields induced by the high-energy laser treatment, phase decomposition occurs in the GNS layer, where the original single-phase BCC TiZrHfTaNb RHEA was gradually decomposed into TiNb-rich BCC phase, TaNb-rich BCC phase, ZrHf-rich HCP phase and TiZrHf-rich FCC phase. In addition, the volume fractions of decomposed phases are gradually increased while the grain size is gradually reduced along the depth direction towards the topmost surface.

(3) The microhardness gradually increases from the original ~ 240 HV to ~ 650 HV in the topmost surface layer, denoting a markedly increment by a factor of ~ 2.7.

(4) The novel laser surface treated GNS TiZrHfTaNb RHEA specimen demonstrates the significantly improved wear resistance. Particularly, the wear rate in the laser-treated GNS TiZrHfTaNb HEA layer is reduced markedly by an order of magnitude, compared with the as-cast alloy. The mixed wear mechanisms including abrasive wear, oxidation wear and adhesive wear are present in both specimens. Nonetheless, the wear is much alleviated in the laser-treated alloy. The decomposed multi-phases and GNS are discussed to achieve the cooperative effect for the significantly improved wear resistance in the GNS TiZrHfTaNb RHEA.

ASSOCIATED CONTENT

Supplementary Material

Figure S1. Optical images of the cross-section (ND-LD) for TiZrHfTaNb RHEAs under different laser powers: (a) 30 W; (b) 60 W; (c) 90 W; (d) 130 W; (e) 160 W; (f) 190 W. (hardened zones are marked by the black dash lines.)

Figure S2. Variations of microhardness along the depth direction in the laser-treated TiZrHfTaNb RHEAs under different laser powers: (a) 30 W; (b) 60 W; (c) 90 W; (d) 130 W; (e) 160 W; (f) 190 W.

Figure S3. TEM characterization of the region at the depth of 10-20 μm below the surface. (a) Bright-field TEM image; (b) Grain size distribution.

Figure S4. Wear debris of TiZrHfTaNb RHEAs after dry sliding against Si_3N_4 balls under 24 N at room temperature. (a) and (c) are SEM image of the wear debris of as-cast alloy and laser-treated alloy, respectively; (b) and (d) are the typical EDS spectra of selected positions in (a) and (c), respectively.

Figure S5. Comparisons of dry-sliding wear performance of laser-treated TiZrHfTaNb in different sliding directions. (a) The COFs as a function of sliding time of laser-treated specimens with sliding directions parallel and vertical to the laser scanning path under different normal loads (16 N, 24 N and 32 N). (b) The wear rates under different normal loads (16 N, 24 N and 32 N). (c) and (d) showing 2D cross-sectional profile along the dotted line (y direction, TD) in the corresponding inset. The insets in (c) and (d) display the 3D profile of wear tracks under 24 N, respectively. (e) and (f) are 3D profiles of worn surface for the laser-treated alloys with sliding direction parallel and vertical to the laser scanning direction, respectively.

Table S1. Wear characteristics of the laser-treated alloys upon dry sliding against Si_3N_4 in different sliding directions.

Figure S6. Surface morphology and composition of the laser-treated alloys after dry sliding against Si_3N_4 under 24 N in different sliding directions. (a) and (d) are SEM images of the worn surfaces of laser-treated alloys with sliding direction parallel and vertical to the laser scanning direction, respectively; The arrows indicate the sliding directions; (b) and (e) are high-magnification SEM images of the selected region in (a) and (d), respectively; (c) and (f) are EDS elemental maps.

Declaration of Competing Interest

The authors declare no conflict of interest.

Acknowledgments

JL was supported by the joint PhD project between the Hong Kong Polytechnic University and Southern University of Science and Technology, and also the grant from the Research Committee of PolyU under student account code RK2N. This work was supported by the National Natural Science Foundation of China Projects (Nos. 51701171 and 51971187) and the Fundamental Research Program of Shenzhen (Grant No. JCYJ20170412153039309).

References

[1] J.W. Yeh, S.K. Chen, S.J. Lin, J.Y. Gan, T.S. Chin, T.T. Shun, C.H. Tsau, S.Y. Chang, Advanced Engineering Materials 6(5) (2004) 299-303.

[2] M.-H. Tsai, J.-W. Yeh, Materials Research Letters 2(3) (2014) 107-123.

[3] H. Huang, Y. Wu, J. He, H. Wang, X. Liu, K. An, W. Wu, Z. Lu, Advanced Materials 29(30) (2017) 1701678.

[4] F. Otto, A. Dlouhy, C. Somsen, H. Bei, G. Eggeler, E. George, Acta Materialia 61 (2013) 5743-5755.

[5] B. Gludovatz, A. Hohenwarter, D. Catoor, E.H. Chang, E.P. George, R.O. Ritchie, Science 345(6201) (2014) 1153.

[6] O.N. Senkov, C. Woodward, D.B. Miracle, JOM 66(10) (2014) 2030-2042.

[7] O.N. Senkov, G.B. Wilks, J.M. Scott, D.B. Miracle, Intermetallics 19(5) (2011) 698-706.

[8] O.N. Senkov, S.L. Semiatin, Journal of Alloys and Compounds 649 (2015) 1110-1123.

[9] E.O. Hall, Proceedings of the Physical Society. Section B 64(9) (1951) 747-753.

[10] N. Petch, J. Iron Steel Inst. Lond. 173 (1953) 25.

[11] O. Senkov, A. Pilchak, S. Semiatin, Metallurgical and Materials Transactions A 49 (2018).

[12] P. Cavaliere, 2015, pp. 3-16.

[13] N. Argibay, T.A. Furnish, B.L. Boyce, B.G. Clark, M. Chandross, Scripta Materialia 123 (2016) 26-29.

[14] S.V. Prasad, C.C. Battaile, P.G. Kotula, Scripta Materialia 64(8) (2011) 729-732.

[15] X. Chen, Z. Han, K. Lu, Wear 320 (2014) 41-50.

[16] X. Zhou, X.Y. Li, K. Lu, Science 360(6388) (2018) 526.

[17] H. Zhao, Z. You, N. Tao, L. Lu, Acta Materialia 210 (2021) 116830.

[18] Z. Cheng, H. Zhou, Q. Lu, H. Gao, L. Lu, Science 362(6414) (2018) eaau1925.

[19] G. Chen, J.W. Qiao, Z.M. Jiao, D. Zhao, T.W. Zhang, S.G. Ma, Z.H. Wang, Scripta Materialia 167 (2019) 95-100.

[20] Z. An, S. Mao, Y. Liu, H. Zhou, Y. Zhai, Z. Tian, C. Liu, Z. Zhang, X. Han, Journal of Materials Science & Technology 92 (2021) 195-207.

[21] S. Yuan, B. Gan, L. Qian, B. Wu, H. Fu, H.-H. Wu, C.F. Cheung, X.-S. Yang, Scripta Materialia 203 (2021) 114117.

[22] S. Wang, S. Wang, H.-H. Wu, Y. Wu, Z. Mi, X. Mao, Science Bulletin 66(10) (2021) 958-961.

[23] W. Xu, X.C. Liu, X.Y. Li, K. Lu, Acta Materialia 182 (2019).

[24] W.L. Li, N. Tao, K. Lu, Scripta Materialia 59 (2008) 546-549.

[25] K. Lu, Science 345(6203) (2014) 1455.

[26] X. Chen, Z. Han, X. Li, K. Lu, Science Advances 2 (2016).

[27] H.W. Huang, Z.B. Wang, J. Lu, K. Lu, Acta Materialia 87 (2015).

[28] N. Tao, Z.B. Wang, W.P. Tong, M. Sui, J. Lu, K. Lu, Acta Materialia 50 (2002) 4603-4616.

[29] H. Shahmir, J. He, Z. Lu, M. Kawasaki, T. Langdon, Materials Science and Engineering: A 676 (2016).

[30] H. Shahmir, M. Nili-Ahmadabadi, A. Shafiee, M. Andrzejczuk, M. Lewandowska, T.G. Langdon, Materials Science and Engineering: A 725 (2018) 196-206.

[31] H. Fu, X. Zhou, B. Wu, L. Qian, X.-S. Yang, Journal of Materials Science & Technology 82 (2021) 227-238.

[32] B. Wu, H. Fu, X. Zhou, L. Qian, J. Luo, J. Zhu, W. Lee, X. Yang, Materials Science and Engineering: A 819 (2021) 141495.

[33] E. Ma, T. Zhu, Materials Today 20 (2017).

[34] B. Schuh, B. Völker, J. Todt, N. Schell, L. Perrière, J. Li, J.-P. Couzinie, A. Hohenwarter, Acta Materialia 142 (2017).

[35] K. Saeidi, X. Gao, Y. Zhong, Z.J. Shen, Materials Science and Engineering: A 625 (2015).

[36] Y. Yao, X. Li, Y. Wang, W. Zhao, G. Li, R. Liu, Journal of Alloys and Compounds 583 (2014) 43-47.
[37] K. Pan, Y. Yang, S. Wei, H. Wu, Z. Dong, Y. Wu, S. Wang, L. Zhang, J. Lin, X. Mao, Journal of Materials Science & Technology 60 (2021) 113-127.
[38] T. Zhaopeng, H. Liu, J. Jiao, W. Zhou, Y. Yang, X. Ren, Journal of Materials Processing Technology 285 (2020) 116806.
[39] T. Zhang, Q. Fan, X. Ma, W. Wang, K. Wang, P. Shen, J. Yang, L. Wang, Materials Letters 253 (2019).
[40] W. Wu, S. Ni, Y. Liu, M. Song, Journal of Materials Research 31 (2016) 1-9.
[41] Y. Bu, Y. Wu, Z. Lei, X. Yuan, H. Wu, X. Feng, J. Liu, J. Ding, Y. Lu, H. Wang, Z. Lu, W. Yang, Materials Today 46 (2021) 28-34.
[42] X. Li, Z. Jin, Z. Xin, K. Lu, Science 370 (2020) 831-836.
[43] J. Ribis, Y. Carlan, Acta Materialia 60 (2012) 238.
[44] Q. Liu, G. Wang, X. Sui, Y. Liu, X. Li, J. Yang, Journal of Materials Science & Technology 35(11) (2019) 2600-2607.
[45] S. Chen, K.-K. Tseng, Y. Tong, W. Li, C.-W. Tsai, J.-W. Yeh, P.K. Liaw, Journal of Alloys and Compounds 795 (2019) 19-26.
[46] C.-H. Tu, S.-K. Wu, C. Lin, Intermetallics 126 (2020) 106935.
[47] W. Guo, B. Liu, Y. Liu, T. Li, A. Fu, Q. Fang, Y. Nie, Journal of Alloys and Compounds 776 (2019) 428-436.
[48] J. Gubicza, A. Heczel, M. Kawasaki, J.-K. Han, Y. Zhao, Y. Xue, S. Huang, J. Lábár, Journal of Alloys and Compounds 788 (2019).
[49] O. Senkov, C. Woodward, D. Miracle, JOM 66 (2014).
[50] M.T. Tsai, J.C. Huang, W.Y. Tsai, T.H. Chou, C.-F. Chen, T.H. Li, J.S.C. Jang, Intermetallics 93 (2018) 113-121.
[51] D. Tabor, Journal of the Institue of Metals 79 (1951) 67-76.
[52] P. Blau, P. Julian, Tribology International - TRIBOL INT 43 (2010) 1203-1208.
[53] C. Yang, K. Aoyagi, H. Bian, A. Chiba, Materials Letters 254 (2019).
[54] O. Senkov, S. Semiatin, Journal of Alloys and Compounds 649 (2015).
[55] G. Tiwari, R. Mehrotra, Defect and Diffusion Forum 279 (2008) 23-37.
[56] Y. Yifan, Q. Wang, J. Lu, C.T. Liu, Y. Yang, Materials Today 19 (2015).
[57] W. Wu, S. Ni, Y. Liu, M. Song, Journal of Materials Research 31(24) (2016) 3815-3823.
[58] L. Zhang, G. Yu, S. Li, X. He, X. Xie, C. Xia, W. Ning, C. Zheng, Optics & Laser Technology 119 (2019) 105577.
[59] L. Wang, T. Cao, X. Liu, B. Wang, K. Jin, Y. Liang, L. Wang, F. Wang, Y. Ren, J. Liang, Y. Xue, Scripta Materialia 189 (2020) 129-134.
[60] M. Sadeghilaridjani, M. Pole, S. Jha, S. Muskeri, N. Ghodki, S. Mukherjee, Wear 478-479 (2021) 203916.
[61] A. Poulia, E. Georgatis, A. Lekatou, A. Karantzalis, Advanced Engineering Materials 19(2) (2017).
[62] C. Mathiou, A. Poulia, E. Georgatis, A.E. Karantzalis, Materials Chemistry and Physics 210 (2018) 126-135.
[63] M. Pole, M. Sadeghilaridjani, J. Shittu, A. Ayyagari, S. Mukherjee, Journal of Alloys and Compounds 843 (2020) 156004.
[64] Y.X. Ye, C.Z. Liu, H. Wang, T.G. Nieh, Acta Materialia 147 (2018) 78-89.
[65] X. Chen, Z. Han, K. Lu, ACS applied materials & interfaces 10 (2018).
[66] X. Mao, J. Sun, Y. Feng, X. Zhou, X. Zhao, Materials Letters 246 (2019).
[67] P. Wang, Z. Han, K. Lu, Wear 402 (2018).
[68] C. Nagarjuna, H.-J. You, S. Ahn, J.-W. Song, K.-Y. Jeong, B. Madavali, G. Song, Y.-S. Na, J.W. Won, H.-

S. Kim, S.-J. Hong, Applied Surface Science 549 (2021) 149202.
[69] A. Erdemir, Tribology Letters 8 (2012) 97-102.
[70] A. Erdemir, Surface & Coatings Technology - SURF COAT TECH 200 (2005) 1792-1796.

Supplementary Material

Laser surface treatment-introduced gradient nanostructured TiZrHfTaNb refractory high-entropy alloy with significantly enhanced wear resistance

Jiasi Luo[a,b], Wanting Sun[a], Ranxi Duan[b], Wenqing Yang[a], K. C. Chan[a], Fuzeng Ren[b*], and Xu-Sheng Yang [a,c*]

[a]Advanced Manufacturing Technology Research Centre, Department of Industrial and Systems Engineering, The Hong Kong Polytechnic University, Hung Hom, Kowloon, Hong Kong, China

[b]Department of Materials Science and Engineering, Southern University of Science and Technology, Shenzhen, Guangdong 518055, China

[c]The Hong Kong Polytechnic University Shenzhen Research Institute, Shenzhen, Guangdong 518060, China

[*] Corresponding author: xsyang@polyu.edu.hk (X.-S Yang); renfz@sustech.edu.cn (F.Z. Ren)

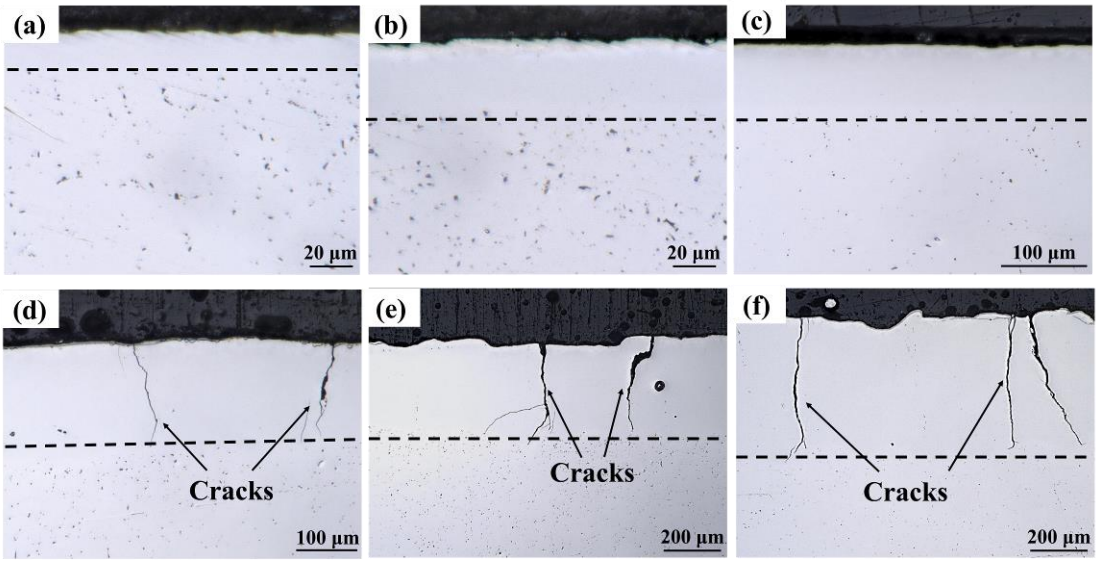

Figure S1. Optical images of the cross-section (ND-LD) for TiZrHfTaNb RHEAs under different laser powers: (a) 30 W; (b) 60 W; (c) 90 W; (d) 130 W; (e) 160 W; (f) 190 W. (hardened zones are marked by the black dash lines.)

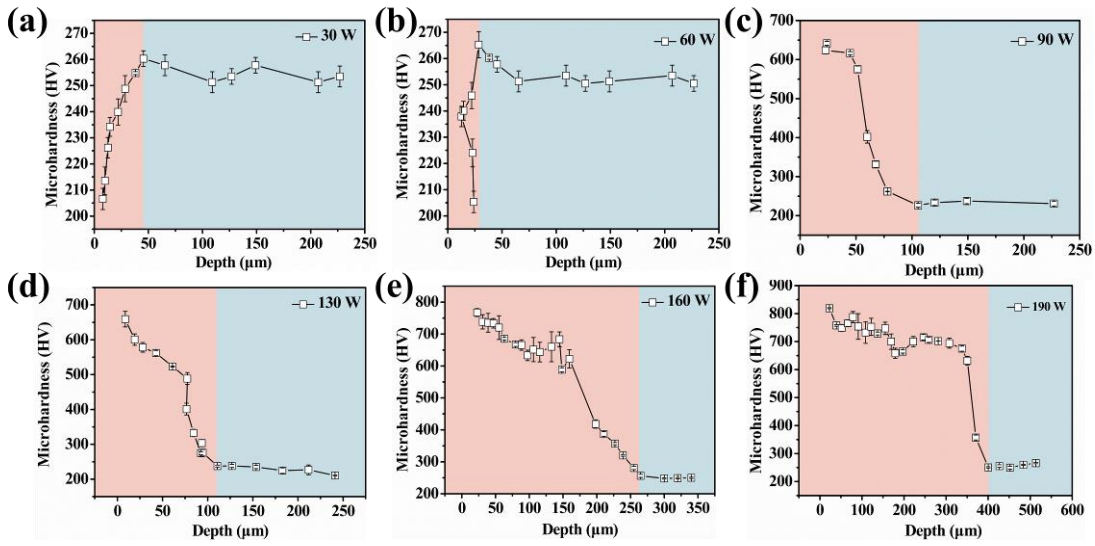

Figure S2. Variations of microhardness along the depth direction in the laser-treated TiZrHfTaNb RHEAs under different laser powers: (a) 30 W; (b) 60 W; (c) 90 W; (d) 130 W; (e) 160 W; (f) 190 W.

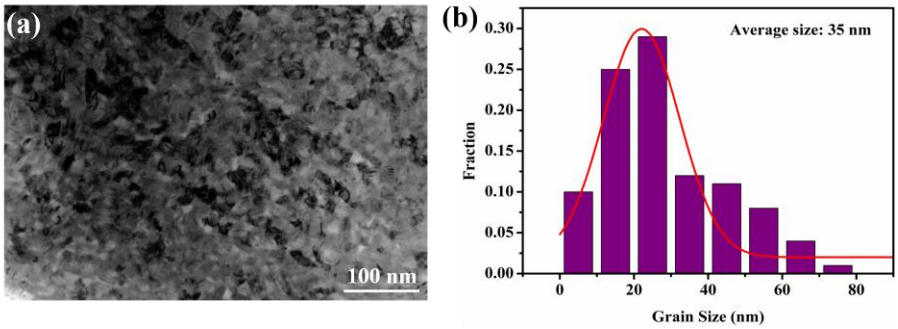

Figure S3. TEM characterization of the region at the depth of 10-20 μm below the surface. (a) Bright-field TEM image; (b) Grain size distribution.

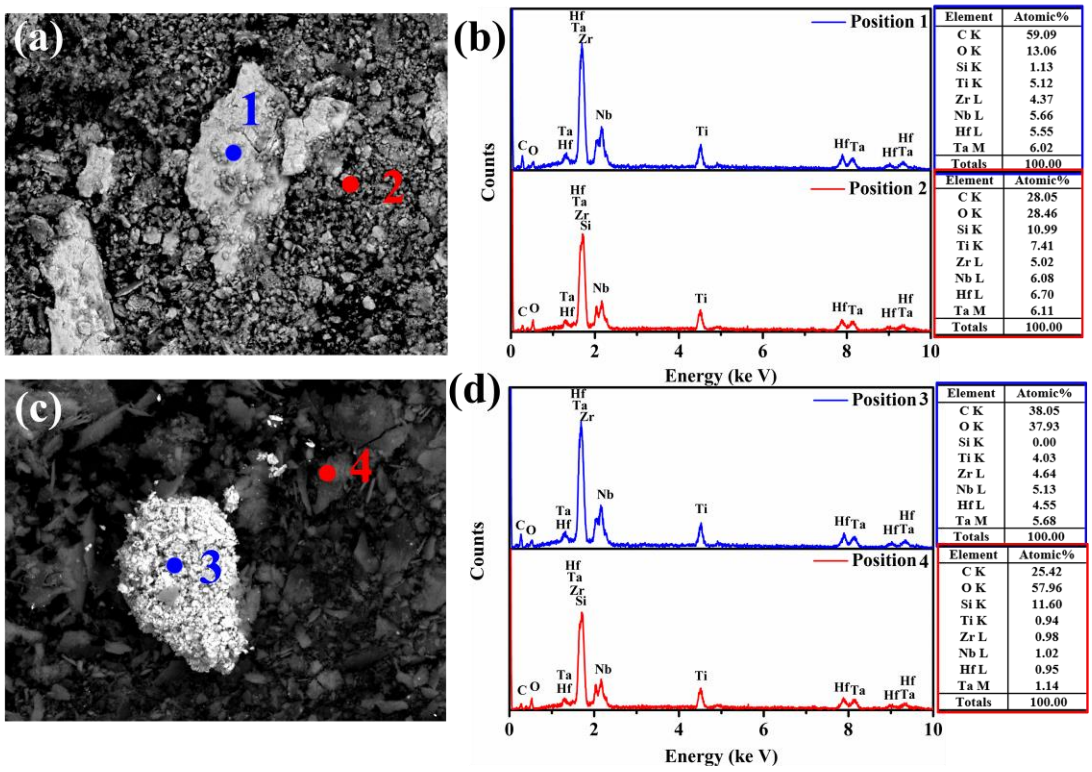

Figure S4. Wear debris of TiZrHfTaNb RHEAs after dry sliding against Si_3N_4 balls under 24 N at room temperature. (a) and (c) are SEM image of the wear debris of as-cast alloy and laser treated alloy, respectively; (b) and (d) are the typical EDS spectra of selected positions in (a) and (c), respectively.

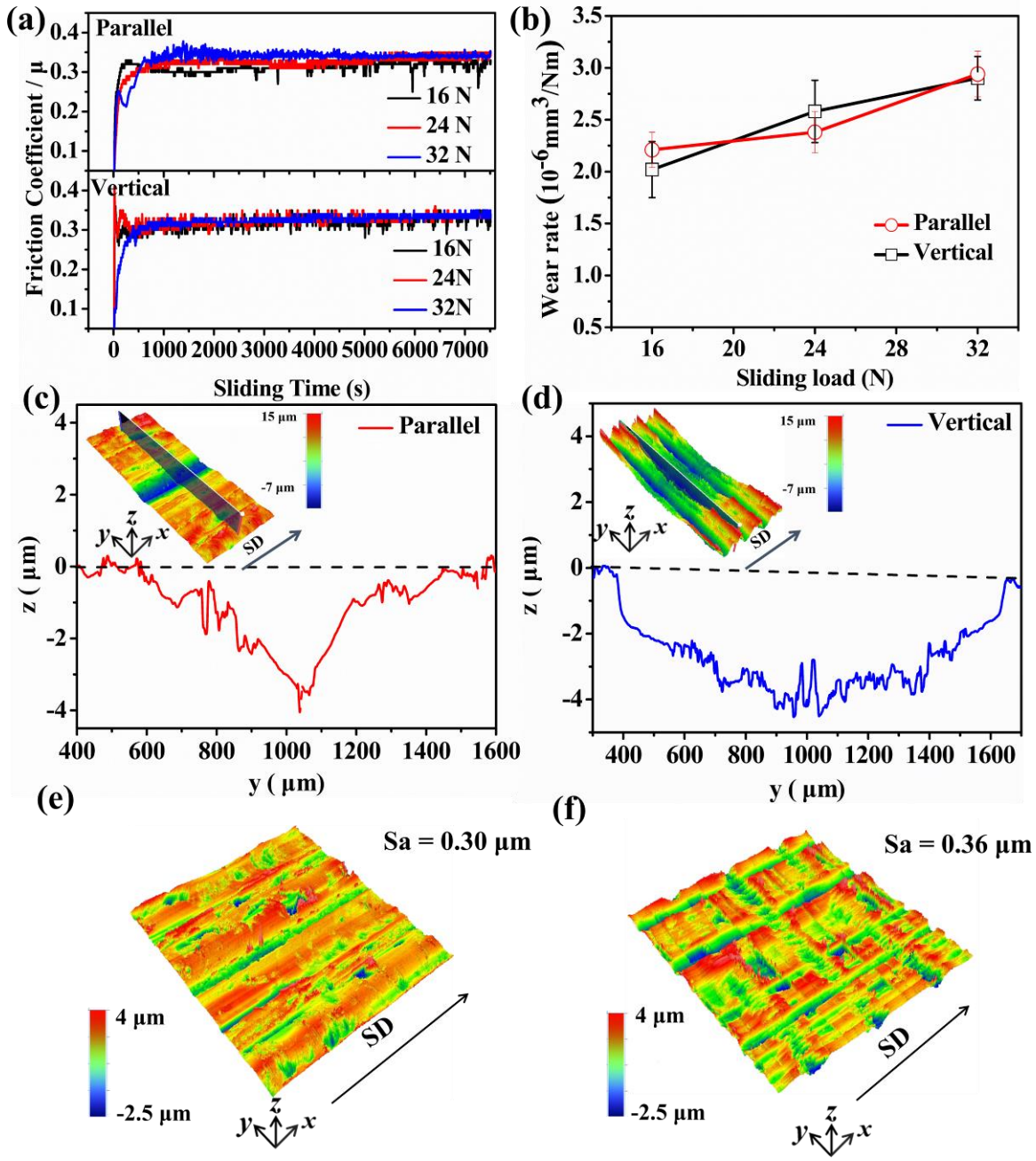

Figure S5. Comparisons of dry-sliding wear performance of laser-treated TiZrHfTaNb in different sliding directions. (a) The CoFs as a function of sliding time of laser-treated specimens with sliding directions parallel and vertical to the laser scanning path under different normal loads (16 N, 24 N and 32 N). (b) The wear rates under different normal loads (16 N, 24 N and 32 N). (c) and (d) showing 2D cross-sectional profile along the dotted line (y direction, TD) in the corresponding inset. The insets in (c) and (d) display the 3D profile of wear tracks under 24 N, respectively. (e) and (f) are 3D profiles of worn surface for the laser-treated alloys with sliding direction parallel and vertical to the laser scanning direction, respectively.

Table S1. Wear characteristics of the laser-treated alloys upon dry sliding against Si_3N_4 in different sliding directions.

Relationship between SD and LD	Normal load (N)	COFs	Wear rate ($mm^3/m \cdot N$)	Wear track roughness /Sa (μm)
Vertical	16	0.32 ± 0.01	2.02 (± 0.27) $\times 10^{-6}$	0.19 ± 0.05
	24	0.33 ± 0.01	2.58 (± 0.30) $\times 10^{-6}$	0.52 ± 0.16
	32	0.34 ± 0.01	2.90 (± 0.21) $\times 10^{-6}$	0.80 ± 0.19
Parallel	16	0.32 ± 0.02	2.21 (± 0.17) $\times 10^{-6}$	0.18 ± 0.07
	24	0.33 ± 0.01	2.38 (± 0.20) $\times 10^{-6}$	0.57 ± 0.17
	32	0.34 ± 0.02	2.94 (± 0.22) $\times 10^{-6}$	0.84 ± 0.20

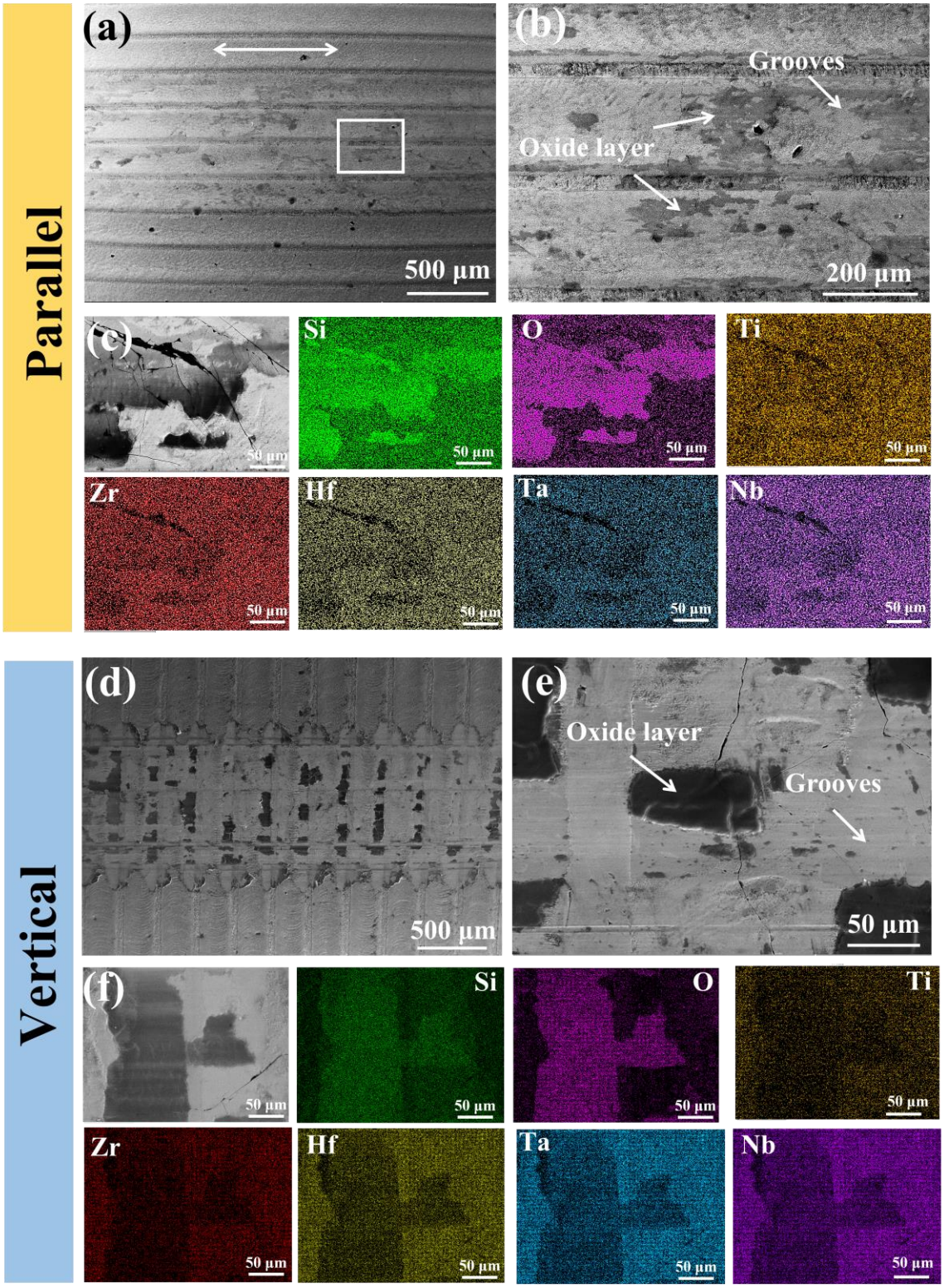

Figure S6. Surface morphology and composition of the laser-treated alloys after dry sliding against Si_3N_4 under 24 N in different sliding directions. (a) and (d) are SEM images of the worn surfaces of laser-treated alloys with sliding direction parallel and vertical to the laser scanning direction, respectively; The arrows indicate the sliding directions; (b) and (e) are high-magnification SEM images of the selected region in (a) and (d), respectively; (c) and (f) are EDS elemental maps.